

special communication

A model of the action potential and underlying membrane currents in a rabbit atrial cell

D. S. LINDBLAD, C. R. MURPHEY, J. W. CLARK, AND W. R. GILES

Department of Electrical and Computer Engineering, Rice University, Houston 77251-1892;

Department of Physiology and Biophysics, University of Texas Medical Branch, Galveston, Texas 77550; and Departments of Medical Physiology and Medicine,

University of Calgary Medical School, Calgary, Alberta, Canada T2N 4N1

Lindblad, D. S., C. R. Murphey, J. W. Clark, and W. R. Giles. A model of the action potential and underlying membrane currents in a rabbit atrial cell. *Am. J. Physiol.* 271 (Heart Circ. Physiol. 40): H1666–H1696, 1996.—We have developed a mathematical model of the rabbit atrial myocyte and have used it in an examination of the ionic basis of the atrial action potential. Available biophysical data have been incorporated into the model to quantify the specific ultrastructural morphology, intracellular ion buffering, and time- and voltage-dependent currents and transport mechanisms of the rabbit atrial cell. When possible, mathematical expressions describing ionic currents identified in rabbit atrium are based on whole cell voltage-clamp data from enzymatically isolated rabbit atrial myocytes. This membrane model is coupled to equations describing Na^+ , K^+ , and Ca^{2+} homeostasis, including the uptake and release of Ca^{2+} by the sarcoplasmic reticulum and Ca^{2+} buffering. The resulting formulation can accurately simulate the whole cell voltage-clamp data on which it is based and provides fits to a family of rabbit atrial cell action potentials obtained at 35°C over a range of stimulus rates (0.2–3.0 Hz). The model is utilized to provide a qualitative prediction of the intracellular Ca^{2+} concentration transient during the action potential and to illustrate the interactions between membrane currents that underlie repolarization in the rabbit atrial myocyte.

atrial myocyte; voltage clamp; Hodgkin-Huxley model

THE SHAPE OF A CARDIAC action potential is determined by the net ionic current resulting from a number of overlapping time- and voltage-dependent inward membrane currents [Na^+ current (I_{Na}) and Ca^{2+} current (I_{Ca})], as well as a number of outward K^+ currents [the “transient outward” K^+ current (I_t), the delayed rectifier current (I_K), and the inward rectifier current (I_{K1})]. In most cardiac cells the large transient inward Na^+ current (I_{Na}) is responsible for the upstroke of the action potential, the smaller and slower inward Ca^{2+} current (I_{Ca}) supports the plateau, and the activation of time- and voltage-dependent K^+ currents initiates and completes repolarization. However, action potentials recorded from isolated cells from various regions of the heart [e.g., atrium, ventricle, Purkinje fibers, and sinoatrial (SA) and atrioventricular (AV) nodes] exhibit different and characteristic waveshapes. To provide a quantitative explanation for these differences, detailed

knowledge of the biophysical properties of the ionic currents in a given type of cell is required.

Enzymatic dispersion techniques, used in combination with whole cell voltage-clamp methods, have provided essential tools for investigating the types and relative sizes of ionic currents in the sarcolemma of single cardiac myocytes (62, 64, 70, 72). Although quantitative data describing the types (selectivity) of ionic currents, as well as their size and kinetics, remain incomplete in many cases, experimental results of this type are available for a number of preparations. These results can be utilized in Hodgkin-Huxley (HH)-type models (59) to provide biophysical explanations for differences in the action potentials in various types of cardiac cells (28, 75–77, 91, 92, 98, 99). However, the data on which such models are based frequently come from a variety of sources and from experiments that are performed under different conditions (e.g., temperature and ionic composition of the bathing medium). Often these voltage-clamp data are incomplete. For example, the steady-state activation and inactivation curves may have been obtained, but the voltage dependence of the associated time constants may not. For this reason, assumptions and approximations have to be made, often resulting in the development of mathematical expressions that estimate the size and kinetics of the current. Although it is possible that quantitative inconsistencies can arise from such an amalgamation of data, HH-type models formed using this approach often produce useful results and yield new insights [e.g., the DiFrancesco and Noble (DN) model]. Ideally, only quantitative, complete voltage-clamp data sets from isolated myocytes should be used as a basis for mathematical descriptions of each ionic current. However, no single laboratory has published quantitative data on each and every type of ionic conductance in a given cardiac cell. Hence, qualitative descriptions of some conductances have to be based on limited available data or results from other tissues or species.

Our model development focuses on a single cell type: the rabbit atrial myocyte. The rabbit atrium has been used extensively in studies of frequency-dependent action potential shape changes (45) and excitation-contraction coupling (56), as well as the mechanism(s) of action of antiarrhythmic agents (64) and metabolic

inhibitors. Moreover, many features of the outward K⁺ currents in rabbit atrium appear to be very similar to those in human atrium (12, 68). Previous work that attempted to characterize the electrical behavior of this cell type (31, 56) used modifications of the DN model of the Purkinje fiber. Hilgemann and Noble (HN) (56) improved this approach by developing expressions for the uptake and release of Ca²⁺ by the sarcoplasmic reticulum (SR). Nevertheless, the DN and HN models contained significant limitations, e.g., 1) they were based on electrophysiological data from multicellular preparations and a number of tissues and 2) they provided an incomplete description of intracellular Ca²⁺ buffering.

The main goal of this work was to develop a mathematical model of the rabbit atrial myocyte based, whenever possible, on quantitative whole cell voltage-clamp data obtained in the laboratory (W. R. Giles) (21, 35, 36, 45, 47, 49, 106). In some cases, data from rabbit atrial myocytes were not available, and data from other cell types were used. In so doing, it is hoped that fundamental properties (e.g., of the Na⁺ channel) would be conserved because of the similarities between cells (e.g., atrial and ventricular myocytes). We resorted to studies from other species only in the few cases in which no suitable rabbit data could be obtained. The resultant semiquantitative model can simulate both the action potential of the rabbit atrial myocyte and individual ionic membrane current waveforms recorded during various voltage-clamp protocols in this cell type. The predictive capability of the model is demonstrated in simulations of whole cell voltage-clamp responses, the typical action potential waveform (APW), the rate-dependent variation of APW with changes in stimulus rate, and intracellular Ca²⁺ concentration ([Ca²⁺]_i) transients. In addition, simulations of the response to "premature" stimuli provide a useful means for attempting to understand the ionic basis for repolarization and the refractoriness of the rabbit atrial myocyte.

Glossary

4-AP	4-Aminopyridine	E_{Na} , $E_{\text{Ca,L}}$, . . .	d_{NaCa}	Denominator constant for I_{NaCa}
APD	Action potential duration			Reversal potential for Na ⁺ channel,
APD ₅₀	Action potential duration measured halfway between RP and POS			long-lasting Ca ²⁺ channel, . . .
APD _{-50mV}	Action potential duration measured at V = -50 mV			Faraday's constant
APW	Action potential waveshape			Inactivation gating variable for $I_{\text{Ca,L}}$
AV	Atrioventricular			Inactivation gating variable for $I_{\text{Ca,T}}$
C _m	Whole cell membrane capacitance			Relative amount of inactive precursor in SR release compartment
[Ca ²⁺] _{up}	Ca ²⁺ concentration in uptake compartment			Relative amount of activator in SR release compartment
[Ca ²⁺] _{rel}	Ca ²⁺ concentration in release compartment			Relative amount of inactive product in SR release compartment
CICR	Ca ²⁺ -induced Ca ²⁺ release			Na ⁺ channel conductance, long-lasting Ca ²⁺ channel conductance, . . .
[Cl ⁻] _{pipette}	Cl ⁻ concentration of solution in pipette			Scaling factor for I_{NaCa}
d_L	Activation gating variable for $I_{\text{Ca,L}}$			Fast inactivation gating variable for I_{Na}
d_T	Activation gating variable for $I_{\text{Ca,T}}$			Slow inactivation gating variable for I_{Na}
g_{Na} , $g_{\text{Ca,L}}$, . . .				Net fractional availability of I_{Na} channels, I_t channels, . . .
h_{total} , s_{total} , . . .				Background current ($I_{\text{B,Na}} + I_{\text{B,Ca}} + I_{\text{B,Cl}}$)
I_B				Ca ²⁺ background current
$I_{\text{B,Ca}}$				Cl ⁻ background current
$I_{\text{B,Cl}}$				Na ⁺ background current
$I_{\text{B,Na}}$				Ca ²⁺ current ($I_{\text{Ca,L}} + I_{\text{Ca,T}}$)
\bar{I}_{Ca}				Long-lasting Ca ²⁺ current
$I_{\text{Ca,L}}$				Transient Ca ²⁺ current
$I_{\text{Ca,T}}$				Ca ²⁺ pump current
\bar{I}_{CaP}				Maximum Ca ²⁺ pump current
\bar{I}_{CaP}				Delayed rectifier K ⁺ current ($I_{\text{K,fast}} + I_{\text{K,slow}}$)
I_K				Fast subtype of delayed rectifier K ⁺ current
$I_{\text{K,r}}$				Slow subtype of delayed rectifier K ⁺ current
$I_{\text{K,s}}$				Inward rectifier K ⁺ current
I_{K1}				Na ⁺ current
I_{Na}				Na ⁺ /Ca ²⁺ exchanger current
I_{NaCa}				Na ⁺ -K ⁺ pump current
\bar{I}_{NaK}				Maximum Na ⁺ -K ⁺ pump current
I_{rel}				SR release compartment current
I_t				Transient outward K ⁺ current
I_{tr}				SR transfer current
I_{up}				SR uptake compartment current
I_V				Current-voltage
k				Slope factor
	[K ⁺] _i , [Na ⁺] _i , [Ca ²⁺] _i , [Mg ²⁺] _i , [Cl ⁻] _i , [K ⁺] _o , [Na ⁺] _o , [Ca ²⁺] _o , [Cl ⁻] _o		K ⁺ , Na ⁺ , Ca ²⁺ , Mg ²⁺ , Cl ⁻ concentrations in intracellular medium	
				K ⁺ , Na ⁺ , Ca ²⁺ , Cl ⁻ concentrations in extracellular bathing medium
			k_{act}	Activation rate constant for gating of I_{rel}
			k_{inact}	Inactivation rate constant for gating of I_{rel}
			k_{off}	Dissociation rate constant for ligand binding
			k_{on}	Association rate constant for ligand binding

k_{recov}	Recovery from inactivation rate constant for gating of I_{rel}	Vol_{up}	Volume of uptake compartment
$K_{\text{cy,Ca}}$	Equilibrium binding Ca^{2+} concentration on cytosol side	z	Valence of ion
K_d	Dissociation constant	$\alpha_m, \alpha_{f_L}, \dots$	Voltage-dependent opening rate constant of m, f_L, \dots
K_{m,Na_i}	Equilibrium binding constant for Na^+ activation of I_{NaK}	α_{up}	Forward reaction rate constant between cytosol and uptake compartment
K_{m,K_o}	Equilibrium binding constant for K^+ activation of I_{NaK}	$\beta_m, \beta_{f_L}, \dots$	Voltage-dependent closing rate constant of m, f_L, \dots
$K_{m,\text{K}1}$	Equilibrium binding constant for $[\text{K}^+]_o$ dependence of $I_{\text{K}1}$	β_{up}	Backward reaction rate constant between cytosol and uptake compartment
$K_{\text{M,rel}}$	Equilibrium binding constant of SR Ca^{2+} release gate for $[\text{Ca}^{2+}]_i$	γ	Position of Eyring rate theory energy barrier controlling voltage dependence of I_{NaCa}
$K_{\text{sr,Ca}}$	Equilibrium binding Ca^{2+} concentration on uptake side	$\Phi_{[\text{Ca}^{2+}]_i}$	Rate of flux of Ca^{2+} onto intracellular buffers
K_{xs}	Translocation constant	ϕ_F	Forward term in voltage dependence of I_{NaCa}
m	Activation gating variable for I_{Na}	ϕ_R	Reverse term in voltage dependence of I_{NaCa}
$\bar{m}, \dot{f}_L, \dots$	Steady state of m, f_L, \dots	$\tau_m, \tau_{f_L}, \dots$	Voltage-dependent time constant of m, f_L, \dots
$dm/dt, \dots$	First time derivative of m, f_L, \dots		
$df_L/dt, \dots$			
MDP	Maximum diastolic potential		
n	Activation gating variable for $I_{\text{K},s}$		
n_{NaCa}	Coupling ratio for $\text{Na}^+/\text{Ca}^{2+}$ exchanger		
$[\dot{\text{Na}}^+]_i, [\dot{\text{K}}^+]_i, \dots$	First time derivative of intracellular concentration of $\text{Na}^+, \text{K}^+, \dots$		
O_c	Fractional occupancy of calmodulin by Ca^{2+}		
O_{Calse}	Fractional occupancy of calsequestrin by Ca^{2+}		
O_{TC}	Fractional occupancy of troponin-Ca complex by Ca^{2+}		
O_{TMgC}	Fractional occupancy of troponin-Mg complex by Ca^{2+}		
O_{TMgMg}	Fractional occupancy of troponin-Mg complex by Mg^{2+}		
$\dot{O}_c, \dot{O}_{\text{TC}}, \dots$	First time derivative of $O_c, O_{\text{TC}}, \dots$		
p_a	Activation gating variable for $I_{\text{K},r}$		
p_i	Inactivation gating variable for $I_{\text{K},r}$		
P_{Na}	Na^+ permeability		
POS	Peak overshoot potential		
R	Universal gas constant		
r	Activation gating variable for I_t		
R_{in}	Input resistance		
RP	Resting potential		
s_1	Fast inactivation gating variable for I_t		
s_2	Slow inactivation gating variable for I_t		
s_3	Third inactivation gating variable for I_t		
SA	Sinoatrial		
SR	Sarcoplasmic reticulum		
T	Temperature (Kelvin)		
$\frac{V}{V_{\text{ss}}}$	Membrane potential for which steady-state gating variable is 0.5		
V	Transmembrane potential (voltage)		
\dot{V}_{max}	Maximum upstroke velocity		
Vol_{Ca}	Intracellular volume for Ca^{2+}		
Vol_i	Intracellular volume		
Vol_{rel}	Volume of release compartment		

MODEL DEVELOPMENT

Our model consists of two components: an equivalent circuit corresponding to the sarcolemma (Fig. 1A) and a fluid compartment model of the intra- and extracellular media of the cell (Fig. 1B). The sarcolemma is treated

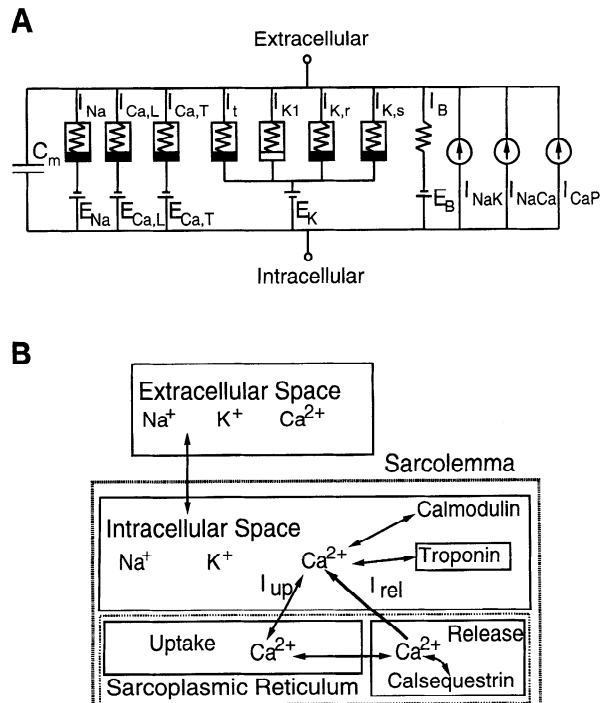


Fig. 1. Components of atrial model. A: membrane equivalent circuit. Boxes around resistors indicate voltage-dependent conductances; filled portion of boxes indicate time-varying conductances. B: fluid compartment model. $[\text{Ca}^{2+}]_i$ is buffered by calmodulin and troponin in cytosol and by calsequestrin in release compartment of sarcoplasmic reticulum. See Glossary for definition of abbreviations.

as a capacitor (C_m , in pF) shunted by several ionic currents, pumps, and exchangers, each of which has been identified in the rabbit atrial cell membrane. These include a fast Na^+ current (I_{Na}), a transient outward K^+ current (I_t), two Ca^{2+} currents ($I_{\text{Ca},\text{T}}$ and $I_{\text{Ca},\text{L}}$), an inwardly rectifying K^+ current (I_{K1}), two delayed rectifier K^+ currents ($I_{\text{K},\text{r}}$ and $I_{\text{K},\text{s}}$), a background current (I_B) consisting of two linear components [a Na^+ ($I_{B,\text{Na}}$) and a Ca^{2+} ($I_{B,\text{Ca}}$) current] and an outwardly rectifying Cl^- current ($I_{B,\text{Cl}}$), a Na^+/K^+ pump current (I_{NaK}), a Ca^{2+} pump current (I_{CaP}), and a $\text{Na}^+/\text{Ca}^{2+}$ exchanger current (I_{NaCa} ; Table 1). Under "space-clamp" conditions, where transmembrane potential (V) is spatially uniform (but time varying), the net ionic current (I_{net}) is linearly related to the time derivative of membrane potential, i.e.

$$I_{\text{net}} = \sum I_{\text{ionic}} = -C_m \frac{dV}{dt} \quad (1)$$

Our model uses HH-based expressions (59) to describe each ionic current; these have the general form

$$I_i = \bar{g}_i y_{i,1}^{k_1} \cdots y_{i,n}^{k_n} (V - E_i) \quad (2)$$

where E_i is the reversal (Nernst) potential for the i th species, \bar{g}_i is the maximum achievable whole cell conductance for the i th current, and the $y_{i,j}$ terms are HH-type "gating variables" (with exponents k_j) for the i th ionic species, which contribute to the variation of

conductance with time and membrane potential. The conductances \bar{g}_i may vary with time and/or membrane potential (see Fig. 1 legend). In the HH formalism, gating variables follow first-order kinetics described by the equation

$$\frac{dy}{dt}(V, t) = \frac{y_\infty(V) - y(V, t)}{\tau_y(V)} \quad (3)$$

where y_∞ represents the steady-state value of y as a function of V and τ_y is the voltage-dependent time constant of y characterizing the "step response" of y to a square step in membrane potential.

The compartmental model provides for material balances of Na^+ , K^+ , and Ca^{2+} within the intracellular medium and for basic Ca^{2+} -handling functions of the SR. It assumes a single compartment for distribution of Na^+ , K^+ , and Ca^{2+} . Two additional compartments account for the uptake, sequestration, and release of Ca^{2+} by the SR. The model provides expressions for the buffering of intracellular Ca^{2+} by calmodulin and troponin, and a Ca^{2+} -specific (T_C) site and a competitive $\text{Ca}^{2+}\text{-Mg}^{2+}$ (T_{MgC}) site on troponin are described. Buffering of Ca^{2+} within the SR release compartment by calsequestrin is also modeled (Fig. 1).

The handling of Ca^{2+} by the SR is described using a two-compartment model. An appropriate rise in $[\text{Ca}^{2+}]_i$ from basal levels triggers the opening of Ca^{2+} release channels, allowing a unidirectional flux of Ca^{2+} from

Table 1. Data sources in rabbit atrial model

Model	Data Source	Use in Model
I_{Na}	Rabbit atrial myocytes (112) Rabbit Purkinje fibers (24)	$\bar{m}^3, \bar{h}_{\text{total}}, I_{\text{Na}}V$ $V_{1/2}$ shift ($\bar{m}^3, \bar{h}_{\text{total}}$) for 35°C; τ_{h_1}, τ_{h_2} estimates at 35°C
$I_{\text{Ca},\text{T}}$	Rabbit SA nodal myocytes (52, 86)	HH model ($\bar{d}_{\text{T}}, \bar{f}_{\text{T}}, \tau_{d_{\text{T}}}, \tau_{f_{\text{T}}}$)
$I_{\text{Ca},\text{L}}$	Rabbit ventricular myocytes (66; H. Banno and W. R. Giles, unpublished data)	$\bar{d}_{\text{L}}, \tau_{f_{\text{L}}}, I_{\text{Ca},\text{L}}V$
I_t	Rabbit SA nodal myocytes (52) Rabbit SA node (88) Rabbit atrial myocytes (21, 36, 38, 45, 106) Rabbit ventricular myocytes (35, 106)	\bar{d}_{L} $\tau_{d_{\text{L}}}, \tau_{s_1}, \tau_{s_2}, \tau_{s_3}$ $\bar{r}, \tau_r, \tau_{s_1}, \tau_{s_2}, \tau_{s_3}$
$I_{\text{K},\text{r}}$	Rabbit crista terminalis (47) Rabbit SA and AV nodal myocytes (49) Rabbit atrial myocytes (84) Rabbit nodal myocytes (104)	τ_r $\bar{p}_{\text{a}}, \bar{p}_{\text{i}}, I\text{-}V$ $\bar{p}_{\text{a}}, p_{\text{i}}, I\text{-}V$
$I_{\text{K},\text{s}}$	Rabbit ventricle (17, 111) Guinea pig ventricle (103)	HH model ($p_{\text{a}}, p_{\text{i}}$)
I_{K1}	Guinea pig ventricular myocytes (67)	\bar{p}_{a}
I_{NaCa}	Rabbit SA and AV nodal myocytes (49) Rabbit atrial and ventricular myocytes (45, 84, 107)	$\tau_{p_{\text{a}}} (\text{qualitatively})$ HH model (n)
I_{NaK}	Rabbit atrial myocytes (31) Guinea pig ventricular myocytes (42, 43, 41)	$I_{\text{K1}}V$ $n_{\text{NaCa}}, k_{\text{NaCa}}, d_{\text{NaCa}}, I_{\text{NaCa}}V$
I_{CaP}	Canine ventricular myocytes (23) Rabbit cardiac myocytes (61)	γ $K_{\text{m},\text{K_o}}, \bar{I}_{\text{NaK}}$
Ca^{2+} buffers	Calf heart (18) Canine ventricular myocytes (100, 108) Skeletal myocytes (97) Frog skeletal myocytes (15, 78) Rabbit skeletal myocytes (94)	K_{m} $k_{\text{on}}, k_{\text{off}}, K_d$ Troponin K_d
Ionic composition	Canine heart myocytes (82) Rabbit ventricular myocytes (27)	Calsequestrin $k_{\text{on}}, k_{\text{off}}$
Ultrastructure	Rabbit atrial and ventricular myocytes (46)	Calsequestrin K_d
	Rat ventricle (95)	Calsequestrin K_d [$\text{Na}^+]$, [K^+] $_i$ Myocyte geometry Compartmental volumes

Table 2. Na^+ current

$I_{\text{Na}} = P_{\text{Na}} m^3 h_{\text{total}} [\text{Na}^+]_o V \frac{F^2 e^{(V - E_{\text{Na}})F/RT} - 1}{RT \frac{e^{VF/RT} - 1}{e^{VF/RT} + 1}}$	
$\frac{dm}{dt} = \alpha_m(1 - m) - \beta_m m$	$\bar{h}_{\text{total}} = \bar{h}_1 = \bar{h}_2 = \frac{\alpha_h}{\alpha_h + \beta_h}$
$\frac{dh_1}{dt} = (\bar{h}_1 - h_1)/\tau_{h_1}$	$\frac{dh_2}{dt} = (\bar{h}_2 - h_2)/\tau_{h_2}$
$\alpha_m = \frac{-460,000(V + 44.4)}{e^{(V + 44.4)/-12.673} - 1}$	$\beta_m = 18,400,000 e^{(V + 44.4)/-12.673}$
$\alpha_h = 44.900 e^{(V + 66.9)/-5.570}$	$\beta_h = \frac{1,491,000}{1 + 323,300 e^{(V + 94.6)/-12.900}}$
$\tau_{h_1} = \frac{0.03000}{1 + e^{(V + 40.00)/6.000}} + 0.00035$	$\tau_{h_2} = \frac{0.12000}{1 + e^{(V + 60.00)/2.000}} + 0.00295$
$h_{\text{total}} = 0.635h_1 + 0.365h_2$	

the release compartment of the SR into the myoplasm. An active extrusion pump returns Ca^{2+} to the SR uptake compartment; thereafter, Ca^{2+} moves to the release compartment via passive diffusion. Calsequestrin molecules located in the release compartment enhance the Ca^{2+} storage capacity of the SR and modify the Ca^{2+} release waveform.

The complete set of equations describing the membrane and fluid compartment models is given in Tables 2–13. Associated parameter values and initial condi-

tions are specified in Tables 14 and 15, respectively. The sarcolemmal currents of the model are discussed in MODEL DEVELOPMENT. Unless otherwise indicated, Tables 2–15, together with Eq. 1, provide a sufficient mathematical context to simulate the model-generated results of this study. A more detailed explanation of the computational aspects involved in model simulations is provided in APPENDIX A.

SARCOLEMMAL CURRENTS

The currents included in our model are those that are known to contribute to the action potential in the rabbit atrial myocyte on the basis of whole cell voltage-clamp data. These include six time- and voltage-dependent currents (I_{Na} , I_t , $I_{\text{Ca,L}}$, $I_{\text{Ca,T}}$, $I_{\text{K,r}}$, and $I_{\text{K,s}}$) and seven background, pump, and exchanger currents (I_{K1} , I_{NaK} , $I_{\text{B,Na}}$, $I_{\text{B,Ca}}$, $I_{\text{B,Cl}}$, I_{CaP} , and I_{NaCa}). The mathematical descriptions of each of these ionic currents (and most background currents) are based on whole cell voltage-clamp data, the sources of which are summarized in Table 1. The data derive predominantly from enzymatically isolated rabbit cardiac myocytes, with many of these results being obtained from atrial myocytes. These currents are discussed below.

Na^+ Current

Na^+ channels generate the large very fast inward current responsible for the initial upstroke (depolarization) of the action potential. The size and speed of I_{Na}

Table 3. Ca^{2+} currents

$I_{\text{Ca}} = I_{\text{Ca,L}} + I_{\text{Ca,T}}$	
$I_{\text{Ca,L}} = g_{\text{Ca,L}}(d_L f_L + d')(V - E_{\text{Ca,L}})$	
$\frac{dd_L}{dt} = (\bar{d}_L - d_L)/\tau_{d_L}$	$\frac{df_L}{dt} = (\bar{f}_L - f_L)/\tau_{f_L}$
$\alpha_{d_L} = \frac{-16.720(V + 35.0)}{e^{(V + 35.0)/-2.500} - 1} + \frac{-50.000V}{e^{V/-4.808} - 1}$	$\beta_{d_L} = \frac{4.480(V - 5.0)}{e^{(V - 5.0)/2.500} - 1}$
$\tau_{d_L} = \frac{1}{\alpha_{d_L} + \beta_{d_L}}$	$\bar{d}_L = \frac{1.000}{1 + e^{(V + 0.95)/-6.600}}$
$\tau_{f_L} = 0.211 \exp \left[-\left(\frac{(V + 37.427)^2}{20.213} \right) \right] + 0.015$	$\bar{f}_L = \frac{\alpha_{f_L}}{\alpha_{f_L} + \beta_{f_L}}$
$\alpha_{f_L} = \frac{8.490(V + 28.0)}{e^{(V + 28.0)/4.000} - 1}$	$\beta_{f_L} = \frac{67.922}{1 + e^{(V + 28.0)/-4.000}}$
$d' = \frac{1.000}{1 + e^{(V - 33.0)/-12.000}}$	
$I_{\text{Ca,T}} = g_{\text{Ca,T}} d_T f_T (V - E_{\text{Ca,T}})$	
$\frac{dd_T}{dt} = (\bar{d}_T - d_T)/\tau_{d_T}$	$\frac{df_T}{dt} = (\bar{f}_T - f_T)/\tau_{f_T}$
$\alpha_{d_T} = 674.173 e^{(V + 23.0)/30.000}$	$\beta_{d_T} = 674.173 e^{(V + 23.0)/-30.000}$
$\tau_{d_T} = \frac{1}{\alpha_{d_T} + \beta_{d_T}}$	$\bar{d}_T = \frac{1.000}{1 + e^{(V + 23.0)/-6.100}}$
$\alpha_{f_T} = 9.637 e^{(V + 75.0)/-83.333}$	$\beta_{f_T} = 9.637 e^{(V + 75.0)/15.385}$
$\tau_{f_T} = \frac{1}{\alpha_{f_T} + \beta_{f_T}}$	$\bar{f}_T = \frac{\alpha_{f_T}}{\alpha_{f_T} + \beta_{f_T}}$

Table 4. Transient outward current

$I_t = g_t r(0.590s_1^3 + 0.410s_2^3)(0.600s_3^6 + 0.400)(V - E_K)$
$\frac{dr}{dt} = (\bar{r} - r)/\tau_r \quad \alpha_r = 386.6 \exp(V/12.00)$
$\frac{ds_1}{dt} = (\bar{s}_1 - s_1)/\tau_{s_1} \quad \beta_r = 8.011 \exp(V/-7.20)$
$\frac{ds_2}{dt} = (\bar{s}_2 - s_2)/\tau_{s_2} \quad \tau_{s_1} = \frac{0.189}{1 + e^{(V+32.80)/0.10}} + 0.0204$
$\frac{ds_3}{dt} = (\bar{s}_3 - s_3)/\tau_{s_3} \quad \tau_{s_2} = \frac{5.750}{1 + e^{(V+32.80)/0.10}}$
$\bar{r} = \frac{1.0}{1 + e^{(V+15.00)/-5.633}} \quad \tau_{s_3} = \frac{7.500}{1 + e^{(V+23.00)/0.5000}} + 0.5000$
$\tau_r = \frac{1}{\alpha_r + \beta_r} + 0.00040$
$\bar{s}_1 = \frac{1.0}{1 + e^{(V+28.29)/7.06}} \quad \bar{s}_3 = \left[\frac{1.0}{1 + e^{(V+50.67)/27.38}} + 0.666 \right] / 1.666$
$\bar{s}_2 = \frac{1.0}{1 + e^{(V+28.29)/7.06}} \quad s_{\text{total}} = (0.59s_1^3 + 0.41s_2^3)(0.60s_3^6 + 0.40)$

activation make its accurate measurement difficult, and voltage-clamp recordings with adequate voltage control must be performed at cold temperatures and/or reduced Na^+ gradients (see Ref. 40 for review). As a result, the steady-state gating or peak current-voltage (I - V) behavior of I_{Na} is often published in the absence of corresponding information on channel kinetics. Consequently, the properties of I_{Na} must be approximated and then mathematically extrapolated to simulate I_{Na} under physiological conditions.

Table 5. Delayed rectifier

$I_K = I_{K,\text{fast}} + I_{K,\text{slow}}$	
$I_{K,\text{fast}} = g_{K,\text{fast}} p_a p_i (V - E_K)$	
$\frac{dp_a}{dt} = (\bar{p}_a - p_a)/\tau_{p_a}$	$\frac{dp_i}{dt} = (\bar{p}_i - p_i)/\tau_{p_i}$
$\alpha_{p_a} = 9.00e^{V/25.371}$	$\beta_{p_a} = 1.3e^{V/-13.026}$
$\tau_{p_a} = \frac{1}{\alpha_{p_a} + \beta_{p_a}}$	$\bar{p}_a = \frac{1.000}{1 + e^{(V+5.1)/-7.400}}$
$\alpha_{p_i} = 100.0e^{V/-54.645}$	$\beta_{p_i} = 656.0e^{V/106.157}$
$\tau_{p_i} = \frac{1}{\alpha_{p_i} + \beta_{p_i}}$	$\bar{p}_i = \frac{\alpha_{p_i}}{\alpha_{p_i} + \beta_{p_i}}$
$I_{K,\text{slow}} = g_{K,\text{slow}} n (V - E_K)$	
$\frac{dn}{dt} = (\bar{n} - n)/\tau_n$	$\bar{n} = \frac{1.000}{1 + e^{(V-0.9)/-13.800}}$
$\alpha_n = 1.66e^{V/69.452}$	$\beta_n = 0.3e^{V/-21.826}$
$\tau_n = \frac{1}{\alpha_n + \beta_n} + 0.060$	

Table 6. Inward rectifier

$I_{K1} = g_{K1} \left(\frac{[\text{K}^+]_o}{[\text{K}^+]_o + K_{m,K1}} \right)^3 \frac{V - E_K}{1 + e^{1.393(V - E_K + 3.6)F/RT}}$
--

Table 7. Background currents

$I_{B,\text{Na}} = g_{B,\text{Na}} (V - E_{\text{Na}})$	$E_{\text{Na}} = \frac{RT}{F} \ln \left(\frac{[\text{Na}^+]_o}{[\text{Na}^+]_i} \right)$
$I_{B,\text{Ca}} = g_{B,\text{Ca}} (V - E_{\text{Ca}})$	$E_{\text{Ca}} = \frac{RT}{2F} \ln \left(\frac{[\text{Ca}^{2+}]_o}{[\text{Ca}^{2+}]_i} \right)$
$I_{B,\text{Cl}} = g_{B,\text{Cl}} (V - E_{B,\text{Cl}})$	$E_{\text{Cl}} = \frac{RT}{F} \ln \left(\frac{[\text{Cl}^-]_{\text{pipette}}}{[\text{Cl}^-]_o} \right)$
	$\cdot \left\{ 1 + \exp \left[\frac{V - (E_{\text{Cl}} + 36.95)}{74.514} \right] \right\}$
$E_{B,\text{Cl}} = E_{\text{Cl}} - 0.49(E_{\text{Cl}} - 30.59)$	$[\text{Cl}^-]_{\text{pipette}} = [\text{Cl}^-]_i$

Table 8. Ca^{2+} pump

$I_{\text{CaP}} = \bar{I}_{\text{CaP}} \frac{[\text{Ca}^{2+}]_i}{[\text{Ca}^{2+}]_i + 0.200 \mu\text{M}}$

Table 9. Na^+ - K^+ pump

$I_{\text{NaK}} = \bar{I}_{\text{NaK}} \left(\frac{[\text{K}^+]_o}{[\text{K}^+]_o + K_{m,K_0}} \right) \left(\frac{[\text{Na}^+]_i^{1.5}}{[\text{Na}^+]_i^{1.5} + K_{m,\text{Na}_i}^{1.5}} \right) \frac{V + 150.0}{V + 200.0}$

Table 10. Na^+ / Ca^{2+} exchanger

$I_{\text{NaCa}} = g_{\text{NaCa}} \frac{([\text{Na}^+]_i^{n_{\text{NaCa}}} [\text{Ca}^{2+}]_o \phi_F - [\text{Na}^+]_o^{n_{\text{NaCa}}} [\text{Ca}^{2+}]_i \phi_R)}{1 + d_{\text{NaCa}} ([\text{Na}^+]_o^{n_{\text{NaCa}}} [\text{Ca}^{2+}]_i + [\text{Na}^+]_i^{n_{\text{NaCa}}} [\text{Ca}^{2+}]_o)}$	
$\phi_F = e^{\gamma V(n_{\text{NaCa}} - 2)z_{\text{NaCa}} F/RT}$	$\phi_R = e^{(\gamma - 1)V(n_{\text{NaCa}} - 2)z_{\text{NaCa}} F/RT}$

Table 11. Intracellular ion concentrations

$[\dot{\text{Na}}^+]_i = - \frac{I_{\text{Na}} + I_{\text{B},\text{Na}} + 3I_{\text{NaK}} + 3I_{\text{NaCa}}}{\text{Vol}_i F}$
$[\dot{\text{K}}^+]_i = - \frac{I_t + I_{\text{K1}} + I_{\text{K}} - 2I_{\text{NaK}}}{\text{Vol}_i F}$
$[\dot{\text{Ca}}^{2+}]_i = - \frac{I_{\text{Ca}} + I_{\text{B},\text{Ca}} + I_{\text{CaP}} - 2I_{\text{NaCa}} + I_{\text{up}} - I_{\text{rel}}}{2\text{Vol}_{\text{Ca}} F} - \Phi_{[\text{Ca}^{2+}]_i}$
$\Phi_{[\text{Ca}^{2+}]_i} = 0.080 \dot{O}_{\text{TrnCa}} + 0.160 \dot{O}_{\text{TrnMgCa}} + 0.045 \dot{O}_{\text{C}}$

Table 12. Intracellular Ca^{2+} buffering

$\dot{O}_{\text{C}} = 200,000.0 [\text{Ca}^{2+}]_i (1 - O_{\text{Cal}}) - 476.0 O_{\text{C}}$
$\dot{O}_{\text{TrnCa}} = 78,400.0 [\text{Ca}^{2+}]_i (1 - O_{\text{TrnCa}}) - 392.0 O_{\text{TrnCa}}$
$\dot{O}_{\text{TrnMgCa}} = 200,000.0 [\text{Ca}^{2+}]_i (1 - O_{\text{TrnMgCa}} - O_{\text{TrnMgMg}}) - 6.60 O_{\text{TrnMgCa}}$
$\dot{O}_{\text{TrnMgMg}} = 2,000.0 [\text{Mg}^{2+}]_i (1 - O_{\text{TrnMgMg}} - O_{\text{TrnMgMg}}) - 666.0 O_{\text{TrnMgMg}}$

Table 13. SR Ca^{2+} handling

$I_{\text{up}} = \bar{I}_{\text{up}} \frac{[\text{Ca}^{2+}]_i / K_{\text{cy,Ca}} - K_{\text{xcs}}^2 [\text{Ca}^{2+}]_{\text{up}} / K_{\text{sr,Ca}}}{([\text{Ca}^{2+}]_i + K_{\text{cy,Ca}}) / K_{\text{cy,Ca}} + K_{\text{xcs}} ([\text{Ca}^{2+}]_{\text{up}} + K_{\text{sr,Ca}}) / K_{\text{sr,Ca}}}$	$I_{\text{rel}} = \alpha_{\text{rel}} \left(\frac{F_2}{F_2 + 0.250} \right)^2 (\text{Ca}^{2+} _{\text{rel}} - \text{Ca}^{2+} _i)$
$I_{\text{tr}} = ([\text{Ca}^{2+}]_{\text{up}} - [\text{Ca}^{2+}]_{\text{rel}}) \frac{2F \text{Vol}_{\text{rel}}}{\tau_{\text{tr}}}$	$[\dot{\text{C}}\text{a}^{2+}]_{\text{rel}} = \frac{I_{\text{tr}} - I_{\text{rel}}}{2 \text{Vol}_{\text{rel}} F} - 31.0 \dot{O}_{\text{Calse}}$
$[\dot{\text{C}}\text{a}^{2+}]_{\text{up}} = \frac{I_{\text{up}} - I_{\text{tr}}}{2 \text{Vol}_{\text{up}} F}$	$\dot{O}_{\text{Calse}} = 480.0 [\text{Ca}^{2+}]_{\text{rel}} (1 - O_{\text{Calse}}) - 400.0 O_{\text{Calse}}$
$\dot{F}_1 = k_{\text{recov}} F_3 - k_{\text{act}} F_1$	$k_{\text{act}} = 203.8 \left(\frac{[\text{Ca}^{2+}]_i}{[\text{Ca}^{2+}]_i + K_{\text{M,rel}}} \right)^4 + 203.8 e^{(V - 40.0)/12.5}$
$\dot{F}_2 = k_{\text{act}} F_1 - k_{\text{inact}} F_2$	$k_{\text{inact}} = 33.96 + 339.6 \left(\frac{[\text{Ca}^{2+}]_i}{[\text{Ca}^{2+}]_i + K_{\text{M,rel}}} \right)^4$
$\dot{F}_3 = k_{\text{inact}} F_2 - k_{\text{recov}} F_3$	

DiFrancesco and Noble (28) developed a formulation for I_{Na} based on Colatsky's (24) two-microelectrode voltage-clamp data obtained at 19°C in multicellular rabbit Purkinje fiber preparations. The DN model used a Goldman-Hodgkin-Katz (GHK) (60) expression to describe the dependence of I_{Na} on V and the Na^+ concentration gradient, and it considered inactivation to follow a single-exponential time course under voltage-clamp conditions and, thus, adopted a traditional HH m^3h form with associated α - β expressions to describe I_{Na} gating. The functionally very significant, although small, slow component of inactivation was not included (24, 28). More recent single-cell studies of cardiac I_{Na} have identified a second component of inactivation and reactivation (20, 39, 80, 101, 112). The faster component accounts for 80–90% of total I_{Na} , and the fast time constant (τ_{fast}) is four to eight times smaller than the slow time constant (τ_{slow}). Given the large size of I_{Na} (≥ 5 nA), a slowly inactivating component responsible for 10% of total current could still supply several hundred picoamperes of inward current during the early plateau. This would be comparable in size to other plateau currents and therefore could play a significant role in determining APW.

Our model of I_{Na} includes fast and slow components of inactivation. We have utilized the perforated patch-clamp data of Wendt et al. (112), which were obtained from enzymatically isolated rabbit atrial myocytes

(17°C), as a basis for descriptions of the steady-state gating and the peak I - V behavior of I_{Na} . Figure 2 summarizes the steady-state and peak I - V properties of I_{Na} in this model. Figure 2A compares the model-generated steady-state activation (\bar{m}^3) and inactivation (\bar{h}_{total}) curves with data from Wendt et al. and Colatsky (24). In our I_{Na} description at 35°C, the steady-state gating variable curves have been shifted to a depolarized position relative to the experimental data. The adjustment in steady-state inactivation corresponds to a +4 mV/10°C shift relative to the –73.5 mV average value of half-inactivation voltage ($V_{1/2}$) stated by Wendt et al. This adjustment compares favorably with the +3 mV/10°C value identified experimentally by Colatsky. We also found that the action potential fits were improved by small reductions in the slope factor for inactivation (obtained from Boltzmann fits to the data in Fig. 2A) from 6.4 mV reported by Wendt et al. to 4.0 mV. A temperature correction of +4.5 mV/10°C (112) was applied to the steady-state activation curve at 35°C, yielding a $V_{1/2}$ of –21.8 mV. In addition, the slope factor was decreased from 8.5 to 7.1 mV. The resulting overlap between the steady-state \bar{m}^3 and \bar{h}_{total} curves is minimal, resulting in a negligible (<2 pA) “window current” (20, 24, 39, 80, 112).

The equations needed for this formulation of I_{Na} are given in Table 2. Many of them are similar to those used

Table 14. Model parameter values

$R = 8314.0 \text{ mJ} \cdot \text{mol}^{-1} \cdot {}^\circ\text{C}^{-1}$	$T = 35.0^\circ\text{C}$	$F = 96487.0 \text{ C/mol}$
$P_{\text{Na}} = 0.0014 \mu\text{l/s}$	$C_m = 0.05 \text{ nF}$	$n_{\text{NaCa}} = 3.0$
$g_{\text{Ca,L}} = 4.000 \text{ nS}$	$\text{Vol}_i = 0.0126 \text{ nl}$	$\gamma = 0.450$
$g_{\text{Ca,T}} = 6.000 \text{ nS}$	$\text{Vol}_{\text{Ca}} = 5.884 \text{ pl}$	$z_{\text{NaCa}} = 1.0$
$g_t = 50.002 \text{ nS}$	$\text{Vol}_{\text{up}} = 0.39690 \text{ pl}$	$d_{\text{NaCa}} = 0.00030$
$g_{\text{K,fast}} = 3.500 \text{ nS}$	$\text{Vol}_{\text{rel}} = 0.04410 \text{ pl}$	$\bar{I}_{\text{up}} = 2800.0 \text{ pA}$
$g_{\text{K,slow}} = 2.500 \text{ nS}$	$[\text{Na}^+]_o = 140.0 \text{ mM}$	$\tau_{\text{tr}} = 0.0100 \text{ s}$
$g_{\text{K1}} = 5.088 \text{ nS}$	$[\text{K}^+]_o = 5.0 \text{ mM}$	$\alpha_{\text{rel}} = 200,000.0 \text{ pA/mM}$
$g_{\text{B,Na}} = 0.064 \text{ nS}$	$[\text{Ca}^{2+}]_o = 2.5 \text{ mM}$	$K_{\text{ey,Ca}} = 0.000030 \text{ mM}$
$g_{\text{B,Ca}} = 0.031 \text{ nS}$	$[\text{Mg}^{2+}]_o = 2.5 \text{ mM}$	$K_{\text{xcs}} = 0.400$
$g_{\text{B,Cl}} = 0.120 \text{ nS}$	$[\text{Cl}^-]_o = 132.0 \text{ mM}$	$K_{\text{sr,Ca}} = 0.500 \text{ mM}$
$\bar{I}_{\text{NaK}} = 64.41 \text{ pA}$	$[\text{Cl}^-]_i = 30.0 \text{ mM}$	$k_{\text{recov}} = 0.815 \text{ s}^{-1}$
$\bar{I}_{\text{Cap}} = 9.509 \text{ nS}$	$K_{\text{m,K}_o} = 1.000 \text{ mM}$	$g_{\text{NaCa}} = 0.020 \text{ nS}$
$E_{\text{Ca,T}} = 38.0 \text{ mV}$	$K_{\text{m,Na}} = 11.000 \text{ mM}$	$K_{\text{M,rel}} = 0.300 \mu\text{M}$
$E_{\text{Ca,L}} = 60.0 \text{ mV}$	$K_{\text{m,K}_i} = 0.590 \text{ mM}$	

Table 15. Initial state values

$V = -69.83663$ mV	$s_2 = 0.39871$	$O_C = 0.02981$
$m = 0.01309$	$s_3 = 0.57363$	$O_{TnCa} = 0.01442$
$h_1 = 0.70600$	$p_a = 0.00016$	$O_{TnMgCa} = 0.23532$
$h_2 = 0.61493$	$p_i = 0.76898$	$O_{TnMgMg} = 0.67476$
$d_l = 0.00003$	$n = 0.02032$	$O_{Calse} = 0.41837$
$f_l = 0.99981$	$[Na^+]_i = 8.40000$ mM	$F_1 = 0.21603$
$d_T = 0.00046$	$[K^+]_i = 100.00000$ mM	$F_2 = 0.00205$
$f_T = 0.30752$	$[Ca^{2+}]_i = 0.07305$ μ M	$F_3 = 0.68492$
$r = 0.00006$	$[Ca^{2+}]_{up} = 0.64913$ mM	
$s_1 = 0.57530$	$[Ca^{2+}]_{rel} = 0.59984$ mM	

in the DN model (28), reflecting the similarity of steady-state curves between the data of Wendt et al. (112) and those of Colatsky (24). As in the DN model, we have used a GHK (60) expression to model the Na^+ and voltage dependence of I_{Na} . However, for simplicity, I_{Na} is assumed to be perfectly selective to Na^+ , and therefore reversal potential corresponds to E_{Na} . Expressions used to describe activation kinetics were also modified from those presented at 19°C in the DN model with use of a Q_{10} of 1.7 (Fig. 2C).

Because of the lack of suitable data describing inactivation kinetics at 35°C in a rabbit preparation, we have approximated τ_{fast} and τ_{slow} for I_{Na} in qualitative terms. The expressions for τ_{h_1} and τ_{h_2} presented in Table 2 (and displayed graphically in Fig. 2, D and E) reflect the relative rates and voltage dependences observed under typical voltage-clamp conditions. At plateau potentials the inactivation time constants are 350 μ s (τ_{h_1}) and 2.8 ms (τ_{h_2}). By comparison, Colatsky (24) estimated a τ_h of 485–728 μ s at 37°C on the basis of a monoexponential decay (at –20 mV). This is consistent with our model, because a monoexponential representation of biexponential data generates a τ value that is intermediate to corresponding dual time constant values. At more hyperpolarized potentials (i.e., near $V_{1/2}$) the inactivation time constants in our model provide acceptable estimates of the relatively slow kinetics of recovery from inactivation typically observed in paired-pulse experiments (48). The τ_{h_1} and τ_{h_2} become faster with depolarization and slower with hyperpolarization, reaching maximum values of 30.3 and 122.8 ms, respectively. The fast reactivation time constant is comparable to the data of Colatsky of 34–48 ms at potentials between –73 and –86 mV. In our model, we have assumed a similar voltage dependence for τ_{h_2} and τ_{h_1} (Fig. 2, D and E). However, τ_{h_2} is ~7.5 times slower at plateau potentials.

Figure 2B illustrates the voltage dependence and current density of I_{Na} in this model. It compares the

peak I - V data of Wendt et al. (Fig. 4B in Ref. 112) at 17°C, normalized to cell capacitance, with the model-generated peak I - V curve at 35°C. The I - V simulation utilized the same voltage-clamp protocol and reduced Na^+ gradient used by Wendt et al. (Fig. 4B in Ref. 112); however, to obtain similar current densities, I_{Na} permeability (P_{Na}) was increased by ~50% over that used in action potential simulations. Overall, the model generates a similar I - V response to the data with minimal ($[Na^+]_o$, P_{Na}) parameter adjustment.

The description of two components of I_{Na} inactivation, one large and fast and the other smaller and slower, suggests that these may play distinct functional roles in influencing APW. Our descriptions of the inactivation gating variables h_1 and h_2 reflect this. As we will show, the fast (h_1 -related) current contributes primarily to the action potential upstroke, whereas the slow (h_2 -related) current interacts late in the upstroke with the early currents of repolarization.

Low-Threshold T-Type Ca^{2+} Current

Bean (3) summarized the experimental evidence for the presence of two types of Ca^{2+} currents in mammalian cardiac myocytes: 1) a high-threshold long-lasting “L-type” ($I_{Ca,L}$) and 2) a low-threshold transient “T-type” ($I_{Ca,T}$) current. $I_{Ca,T}$ and $I_{Ca,L}$ have also been identified in isolated rabbit SA nodal cells by Hagiwara et al. (52) and Nathan (86) using whole cell and cell-attached patch-clamp techniques at 37°C. Hagiwara et al. found that $I_{Ca,T}$ differs from $I_{Ca,L}$ in its activation and inactivation behavior, conductance properties, and sensitivity to blocking agents. In this work the effects of $NiCl_2$ (40 μ M) or tetramethrin (0.1 μ M) were interpreted in terms of a selective block of $I_{Ca,T}$, and nifedipine and D600 were shown to block $I_{Ca,L}$ without affecting $I_{Ca,T}$. Cadmium (20 μ M) and cobalt (2 mM) can inhibit $I_{Ca,T}$ and $I_{Ca,L}$. Hagiwara et al. reported that the current density of $I_{Ca,T}$ in rabbit SA nodal cells is ~10 times larger than that in atrial or ventricular cells. In our simulations $I_{Ca,T}$ has a negligible effect on intracellular Ca^{2+} handling or the APW and provides only a tiny contribution (relative to I_{Na}) to the action potential upstroke. For completeness, we have included equations adapted from Hagiwara et al. for $I_{Ca,T}$ in our model (Table 3); a Q_{10} of 1.8 was used to adjust rate expressions for the gating variables d_T and f_T . However, our simulations and the results of Hagiwara et al. support the view that $I_{Ca,T}$ has minimal functional importance in rabbit atrial myocytes (96).

High-Threshold L-Type Ca^{2+} Current

Depolarization initiates the time- and voltage-dependent activation of a sustained inward L-type Ca^{2+} current ($I_{Ca,L}$). During the action potential, this “long-lasting” current opposes the repolarizing influences of I_K and I_{Na} . Hence, $I_{Ca,L}$ supports the plateau and delays the onset of repolarization. In addition, by increasing $[Ca^{2+}]_i$, $I_{Ca,L}$ provides the trigger for Ca^{2+} -induced calcium-release (CICR) from the SR (33, 34). Because $I_{Ca,L}$ affects excitation and excitation-contraction coupling, accurate quantitative models are needed for complete explanations of the dual roles of $I_{Ca,L}$.

Table 16. Comparison of model output with quiescent cell electrophysiological parameters

Parameter	Value	
	Literature	Model
RP	–71.0 mV	–71.70 mV
R_{in}	617.0 ± 401.0 M Ω	757.5 M Ω
C_m	54.3 ± 5.9 pF	50.00 pF

Literature values are means \pm SD, as cited from Giles and Imaizumi (45).

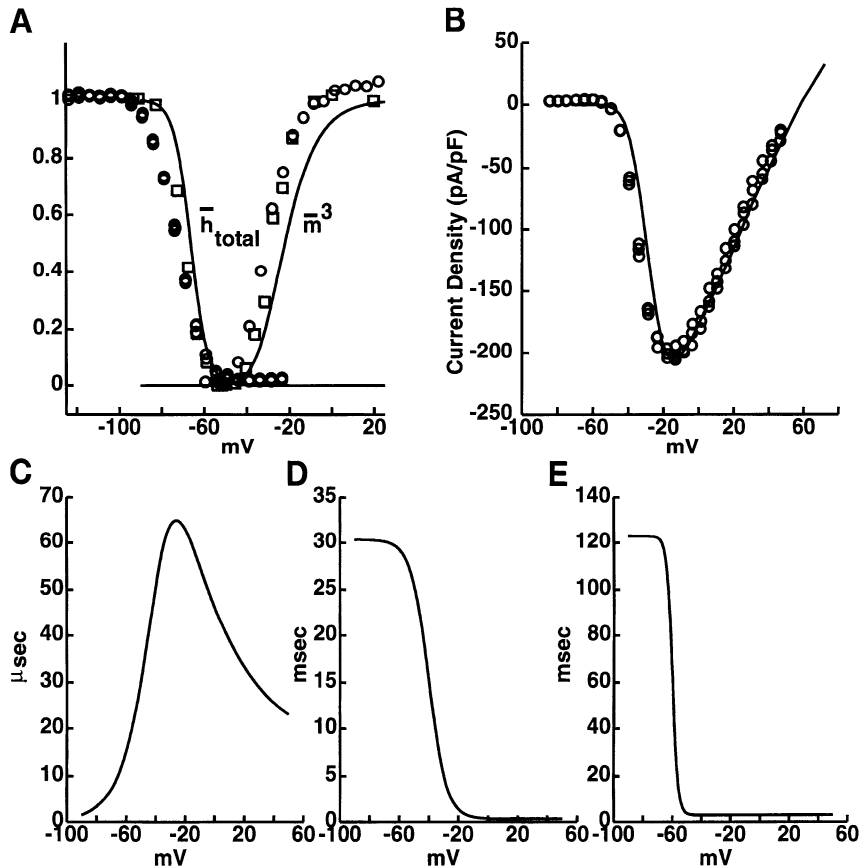


Fig. 2. Parameters used to model I_{Na} . A: steady-state activation (\bar{m}^3) and inactivation (\bar{h}_{total}) curves. Data from Wendt et al. (○, 17°C) [Fig. 4, A (normalized) and B (inset) in Ref. 112] and Collatsky (□, 19°C) (Fig. 5 in Ref. 24) are compared with this model (solid curve, 35°C). B: model-generated (solid curve, 35°C, 50 pF) and recorded (○, 17°C, 14 pF, perforated patch) rabbit atrial peak I - V relations, normalized for cell capacitance, obtained using identical “test pulse” parameters (holding potential = -90 mV, $[\text{Na}^+]_o = 75 \text{ mM}$). Data are from Wendt et al. (Fig. 4B in Ref. 112). Model conductance was rescaled as described in text. C–E: time constants for activation (τ_m) and fast (τ_{h_1}) and slow (τ_{h_2}) inactivation, respectively.

Under voltage-clamp conditions, $I_{\text{Ca,L}}$ is recorded as a transient inward current that is maximal at $\sim 0 \text{ mV}$. The inactivation time course of $I_{\text{Ca,L}}$ is complex and has been reported to follow various patterns of decay (mono-exponential, biexponential, or neither) depending on the temperature, permeant ion, tissue, and species studied (96). Paired-pulse experiments reveal a similarly complicated time course of recovery from inactivation. Whereas Ca^{2+} and membrane potential have been implicated as important factors influencing $I_{\text{Ca,L}}$ inactivation (50, 51), the precise mechanism(s) governing the process of inactivation remains unclear, and the relative importance of each factor in the inactivation process has not been described.

In the absence of detailed quantitative information describing $I_{\text{Ca,L}}$ inactivation, we have adopted a relatively simple model in which inactivation is treated as a time- and voltage-dependent process. Our approach differs, therefore, from that of investigators (28, 76, 77) who have proposed qualitative descriptions of the $[\text{Ca}^{2+}]_i$ - V interaction. Our model uses a single activation (d_L) and inactivation (f_L) gating variable to describe channel gating. The complete expressions (Table 3) are based jointly on data from Hagiwara et al. (52), Nilius (88), H. Banno and W. R. Giles (unpublished observations), and Kawano and Hirooka (66). A Boltzmann function has been used to describe steady-state activation on the basis of data from Hagiwara et al. in 37°C SA nodal cells; however, the $V_{1/2}$ for activation has been shifted by +5.55 mV from results of Hagiwara et al., placing the activation curve closer to that measured

by Banno and Giles in 35°C rabbit ventricular myocytes. Conventional α and β rate constant expressions have been used to obtain steady-state inactivation on the basis of a fit to the data of Hagiwara et al.

In this fit, the Boltzmann equation for the steady-state inactivation predicts complete inactivation at potentials $> 0 \text{ mV}$ (Fig. 3A). This would suggest that $I_{\text{Ca,L}}$ would decline to zero in a suitably long voltage-clamp step to these potentials. Several other “paired-pulse” studies in cardiac preparations (13, 50, 65, 69, 81) have reported steady-state inactivation curves that do not decline to zero but, rather, increase from a small value (e.g., 5% at 0 mV) to a larger value (e.g., $\sim 40\%$) at positive membrane potentials. The phenomenon of “incomplete inactivation” may result from the Ca^{2+} dependence of $I_{\text{Ca,L}}$ inactivation (96). To model this behavior, we have included a noninactivating term (d') in our description of $I_{\text{Ca,L}}$. The term describes a component having a threshold near -25 mV and a $V_{1/2}$ of $+33 \text{ mV}$ (not shown) and is based on paired-pulse measurements in our laboratory.

The data of Hagiwara et al. (52) on $I_{\text{Ca,L}}$ did not include the voltage dependence of the time constants; therefore approximations were used. Our equations for τ_{d_L} have been adapted from Nilius (88), whereas the time constant for inactivation (τ_{f_L}) has been formulated on the basis of data from H. Banno and W. R. Giles (unpublished observations), Hagiwara et al. (52), and Kawano and Hirooka (66). Values of τ_{f_L} at depolarized potentials represent the average time constants resulting from single-exponential fits to $I_{\text{Ca,L}}$ transients re-

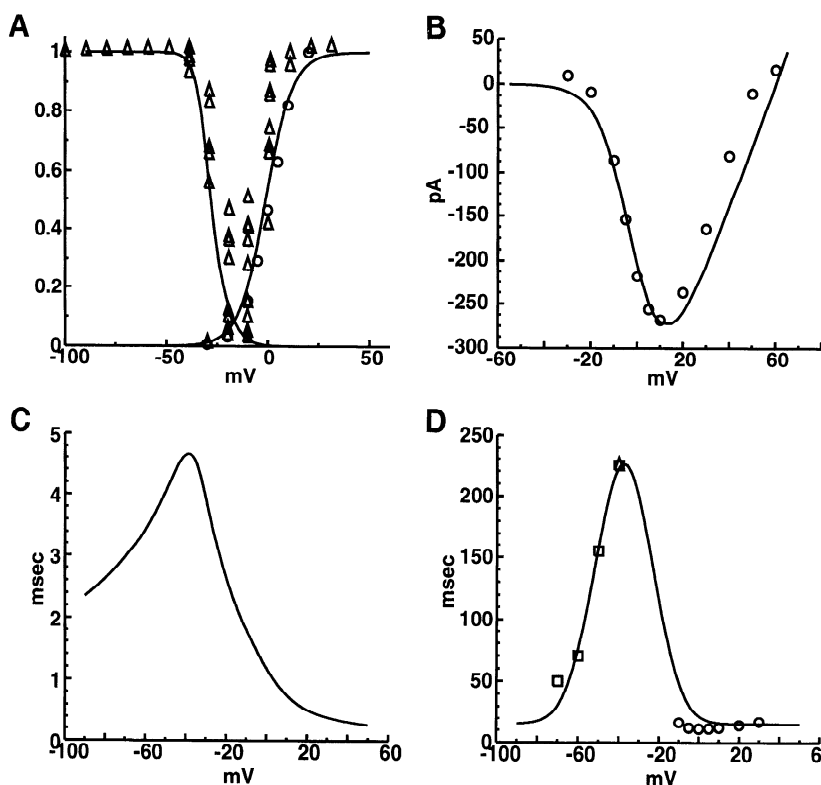


Fig. 3. Parameters used to model L-type Ca^{2+} current. A: steady-state activation (d_L , right) and inactivation (f_L , left) curves. B: model (solid curve) and experimental peak I - V data from holding potential of -75 mV. Data are from Hagiwara et al. (Δ , scaled by 15%) (Fig. 1B in Ref. 52) and H. Banno and W. R. Giles (\circ , current rescaled for 27.5 pF ventricular cell) (unpublished observations). C and D: time constants for activation (τ_{d_L}) and inactivation (τ_{f_L}), respectively. Data are from Kawano (\square) (66), Hagiwara et al. (Δ) (Fig. 8B in Ref. 52), and Banno and Giles (\circ).

corded from 35°C rabbit ventricle. At more hyperpolarized potentials, time constants of recovery from inactivation are from Kawano and Hiroaka. They represent time constants from single-exponential fits of recordings of $I_{\text{Ca,L}}$ at 33 – 35°C in rabbit ventricle.

Figure 3 shows the complete steady-state curves for $I_{\text{Ca,L}}$ at 35°C as well as the model-generated peak I - V responses obtained from a holding potential of -75 mV. As shown in Fig. 3B, the model-generated I - V curve provides an acceptable representation of the experimentally recorded I - V relationship for $I_{\text{Ca,L}}$.

Transient and Steady Outward Currents

A Ca^{2+} -independent transient outward K^+ current (I_t) develops immediately after the action potential upstroke. Its rapid activation kinetics and relatively large conductance allow it to significantly modulate early repolarization. Studies by Boyett et al. (7, 8, 11) and others (12, 45, 74) have correlated variations in APW with the size of I_t .

Voltage-clamp experiments have defined I_t as a large and rapidly activating time- and voltage-dependent K^+ current with complex inactivation and reactivation (i.e., recovery from inactivation) properties (12, 35, 38, 45, 106). In rabbit atrial and ventricular myocytes, I_t can supply hundreds of picoamperes of outward repolarizing current, and peak I_t (when fully recovered from inactivation) is substantially larger than other (I_K , $I_{\text{K,Ca}}$, and $I_{\text{K,Na}}$) outward K^+ currents (35, 38, 45). Other important properties (12) of this current include the following: 1) it is blocked selectively by 4-aminopyridine (4-AP); 2) it is highly temperature sensitive; 3) steady-state activation and inactivation curves mea-

sured by standard protocols vary sigmoidally with membrane voltage; 4) two time constants are required to describe its inactivation and reactivation kinetics, and neither is strongly dependent on membrane potential; 5) reactivation is very slow; and 6) the size of peak current is very sensitive to action potential firing frequency. The latter arises from the slow recovery from inactivation; as long as 30 s may be required to achieve full recovery (38, 106).

Our mathematical description of I_t is based on voltage-clamp studies from two sources: 1) our studies in cardiac myocytes from the rabbit atrium, ventricle, and crista terminalis (12, 21, 35, 36, 46, 47) and 2) studies of Fermini et al. (38) on rabbit atrium. Table 4 gives the equations describing I_t , which include one activation (r) and three inactivation (s_1 , s_2 , and s_3) gating variables to describe the complex voltage- and time-dependent behavior of this current. Figure 4 shows the voltage-dependent steady-state and time constant curves for r , s_1 , s_2 , and s_3 , along with discrete points obtained from voltage-clamp protocols. The data points presented for τ_r , τ_{s_1} , τ_{s_2} , and τ_{s_3} at potentials between -20 and $+20$ mV were obtained from a least squares fit (79) of our mathematical description of I_t to the voltage-clamp records of Fedida and Giles (Fig. 6A in Ref. 35). This has enabled our model to mimic the entire current waveform obtained under voltage-clamp conditions. A suitable fit could not be obtained with the standard practice of fitting only the decay phase of the voltage-clamp transient to a sum of exponentials (14). To fit the voltage-clamp records of Fedida and Giles (Fig. 6A in Ref. 35) and match 35°C atrial action potential repolarization trajectories (A. Braun and W. R. Giles, unpub-

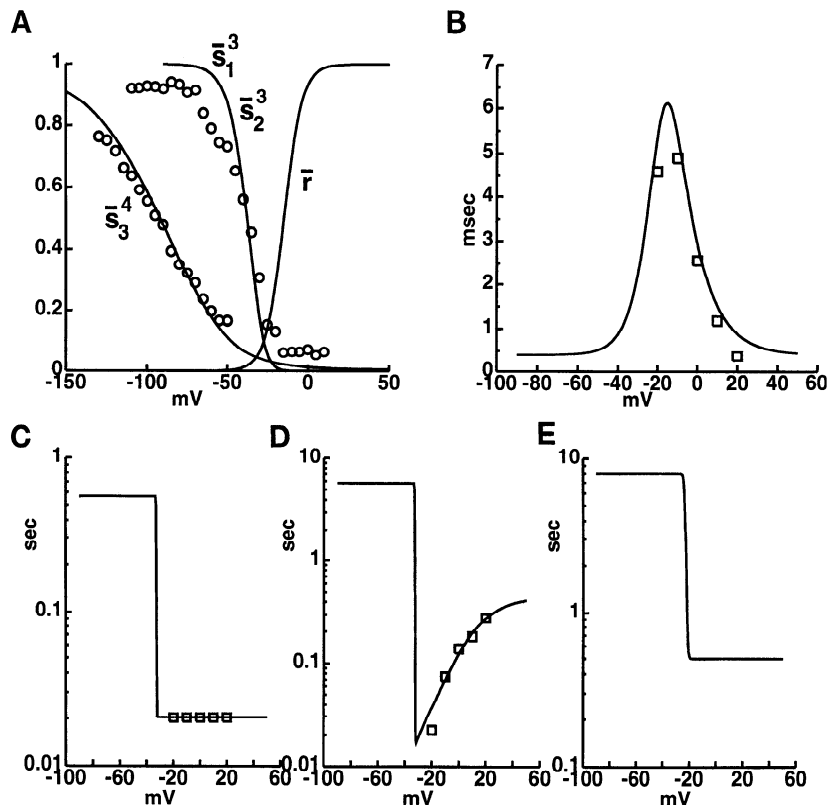


Fig. 4. Parameters used to model transient outward current (I_t). A: steady-state activation (\bar{r}) and inactivation ($\bar{s}_1^3, \bar{s}_2^3, \bar{s}_3^4$) gating variable curves. Data (○) from Fedida et al. [Figs. 9 and 11 in Ref. 36 (rescaled)] have been shifted by -10 mV to correct for tip potential. B–E: time constants for activation (τ_r), fast inactivation (τ_{s1}), slow inactivation (τ_{s2}), and “slow reactivation” (τ_{s3}), respectively. Data points (□) represent discrete measurements from voltage-clamp protocols via least squares parameter estimation of time constants (B–E) with the use of model equations to fit data of Fedida and Giles (Fig. 6 in Ref. 35).

lished data), the steady-state activation curve (\bar{r}) was formulated using a -3.0 -mV shift in the half-activation value and a 70.4% broadening in the slope at half-activation relative to values stated for rabbit atrium at 23°C by Clark et al. (21). Midpoint values and slope factors for the steady-state inactivation of variables s_1 and s_2 were taken directly from the “standard inactivation protocol” measurement of Fedida et al. (Fig. 9 in Ref. 36); corresponding parameters for s_3 were adjusted to achieve a least squares fit to the “cumulative steady-state inactivation” data of Fedida et al. (Fig. 11 in Ref. 36).

Activation of I_t has proven to be difficult to characterize at physiological temperature because of the speed and size of this current (35). In myocytes from rabbit crista terminalis at 23°C (47), τ_r has been found to have a “bell-shaped” dependence on membrane potential, with the peak occurring close to the $V_{1/2}$. Accordingly, we have adopted a Gaussian expression to describe τ_r and then adjusted the parameters to achieve a least squares fit (79) to the ventricular myocyte data of Fedida and Giles at 35°C (35). Compared with the data of Giles and van Ginneken (47), the resultant bell-shaped curve has a narrower voltage dependence, places peak τ_r at a more depolarized potential, and specifies an approximately three times faster value for peak τ_r .

Time constants for the inactivation gating variables reflect the complexity of the inactivation and reactivation processes. At depolarized potentials, τ_{s1} and τ_{s2} represent the two components of inactivation observed for I_t (21). Analytic expressions (Table 4) have been adopted to represent the voltage-dependent behavior of these functions, and the parameters have been

adjusted to achieve least squares fits (79) to inactivation time constants estimated from the whole cell voltage-clamp data of Fedida and Giles (35). Values for time constants at potentials near or below the resting potential (RP) represent the slow multiple time constant reactivation of I_t . Reactivation of I_t has been measured in rabbit atrium at a holding potential of -80 mV (at 23°C) (21, 45, 106) and at V of -60 mV (30°C) (38). It has been found to consist of a slow and a fast component, with time constants of 14.6 and 3.93 s at 23°C and 8.4 and 0.65 s at 30°C , respectively (21, 38, 45, 106). Giles and Imaizumi (45) found no, or very weak, voltage dependence of the recovery time course. Therefore, if voltage dependence is neglected, rate constants can be projected from these values (23 and 30°C) to 35°C with the assumption of an exponential dependence of rate on temperature, i.e.

$$\tau = B \exp \left(\frac{E_a}{RT} \right) \quad (4)$$

where E_a is the activation energy and B is a constant (57, p. 272). With use of this assumption, values for B and E_a may be uniquely determined for each (slow and fast) reactivation process from Eq. 4 and the kinetic data. This calculation yields reactivation time constants of 5.75 s and 189 ms at 35°C , which corresponds to Q_{10} values of 2.18 and 12.75 for slow and fast reactivation, respectively. These values have been used to guide the model-generated diastolic reactivation response (a combined effect of τ_{s1} , τ_{s2} , and τ_{s3}) in the assumed physiological or “warm” condition. Further adjustments have been made in selecting values for τ_{s1} ,

τ_{s_0} , and τ_{s_3} to accurately simulate rate-sensitive behavior of I_t . The somewhat unusual voltage dependences of τ_{s_1} , τ_{s_2} , and τ_{s_3} in Fig. 4, C–E, reflect significant differences in systolic inactivation and diastolic reactivation kinetics of I_t as measured by standard voltage-clamp protocols (35, 106).

In voltage-clamp measurements, the outward current that remains after inward Na^+ and Ca^{2+} currents have been eliminated consistently has a noninactivating steady-state component (29, 35). This steady current can be observed even at plateau potentials where complete inactivation of I_t is expected. The origins of this current have been investigated in rabbit (29, 35) and other species (37, 114). In rabbit preparations, the steady current increases in size with depolarization (29, 35) and is insensitive to 4-AP, 10 mM tetraethylammonium, and rapid stimulation (29, 35, 38). In rabbit atrium it is attenuated by Cl^- transport blockers and is sensitive to Cl^- concentration in the recording pipette (29). On this basis, it was identified as a Cl^- current, although slight deviations in its reversal potential from E_{Cl} suggested that some contamination (e.g., with a K^+ current) may also be present (29). Accordingly, we have formulated a model of the steady current as an instantaneous background Cl^- current ($I_{\text{B},\text{Cl}}$) on the basis of the I - V relation of Duan et al. (Fig. 3A in Ref. 29). Model-generated and experimental I - V data are shown together in Fig. 5. An empirical relation was used to describe its reversal potential ($E_{\text{B},\text{Cl}}$), which accounts for the deviation of $E_{\text{B},\text{Cl}}$ from E_{Cl} (Table 7).

Our models of I_t and $I_{\text{B},\text{Cl}}$ were combined to fit the data of Fedida and Giles (35). Figure 6 shows the model-generated and superimposed experimental data

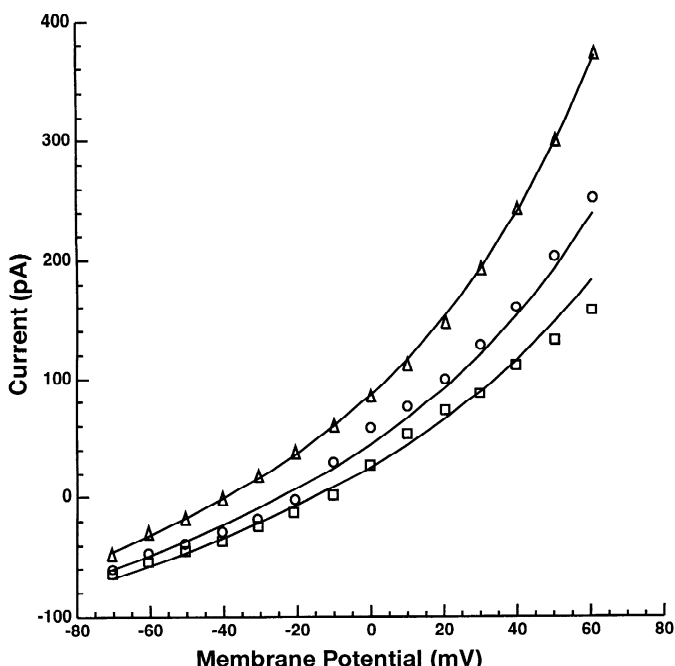


Fig. 5. I - V relation of Cl^- current (I_{Cl}). Model fits (solid curves) to I - V relation of Cl^- current identified by Duan et al. (Fig. 3a in Ref. 29) were parameterized by $[\text{Cl}^-]_{\text{pipette}}$. $[\text{Cl}^-]_{\text{i}}$ is 137.4 mM; $[\text{Cl}^-]_{\text{pipette}}$ is 22 (\triangle), 67 (\circ), or 132 (\square) mM. Model expression (Table 7) assumes complete intracellular dialysis, i.e., $[\text{Cl}^-]_{\text{i}} \sim [\text{Cl}^-]_{\text{pipette}}$.

in response to 400-ms voltage-clamp steps from a holding potential of -80 mV to clamp potentials of -20 , -10 , 0 , $+10$, and $+20$ mV applied at 10-s intervals. The agreement between the data and model suggests that I_t and $I_{\text{B},\text{Cl}}$ provide the majority of the current responsible for the measured response of this cell.

Figure 6, B and C, illustrates two additional tests of the kinetics of the I_t model. In Fig. 6B, the reactivation time course of I_t was tested using a paired-pulse protocol. Data from Fermini et al. (38) in 30°C rabbit atrial myocytes are compared with model-generated responses obtained with a nominal I_t model (35°C) and with a model adjusted to 30°C by use of Q_{10} factors. In the latter, activation kinetics (τ_r) were adjusted using a Q_{10} of 2.3. Inactivation (τ_{s_1} , τ_{s_2} , and τ_{s_3}) kinetic adjustments utilized separate Q_{10} factors for the “inactivating” Boltzmann (Q_{10} of 2.3, 2.3, and 0.1) and “reactivating” offset (Q_{10} of 2.18, 12.75, and 5.0) terms of the time constant expressions. The response of the temperature-adjusted 30°C model agrees qualitatively with the data, although both model-generated responses have a slightly faster slow phase of reactivation than that observed by Fermini et al. (38). Figure 6C compares the rate-dependent availability or “frequency dependence” of I_t (at 36°C) with the data of Duan et al. (29) obtained in rabbit atrial myocytes at 36°C . In Fig. 6C, the peak current (in steady state) elicited by a voltage-clamp step to 0 mV from -60 mV is displayed as a function of the period at which the voltage-clamp protocol is applied. Currents have been normalized by the response at a period (cycle time) of 10 s (0.1 Hz). A similar decline in I_t as frequency is increased is observed in the simulations and data, although the reduction of I_t by high stimulus rates is more complete in the model than in the findings of Duan et al.

Delayed Rectifier

The delayed rectifier K^+ current (I_K) contributes to repolarization in a variety of cardiac cell types (89). Recent studies in guinea pig myocytes (102, 103) have identified fast ($I_{K,r}$) and slow ($I_{K,s}$) delayed rectifier currents, in part on the basis of differential sensitivity to the class III antiarrhythmic agent E-4031. Similar currents have been identified in rabbit SA and AV nodal cells by Habuchi et al. (49) and in rabbit atrial myocytes by Muraki et al. (84). The fast-type I_K current has also been found in rabbit ventricle (17, 22, 111) and rabbit nodal cells (104).

The two types of delayed rectifiers identified in rabbit heart preparations have been shown to possess distinct pharmacological, ion-transfer, and kinetic properties (see Ref. 24 for review). $I_{K,r}$ is blocked selectively by class III antiarrhythmic agents (e.g., sotalol, dofetilide, and E-4031), has an inwardly rectifying ion-transfer characteristic, and has relatively fast activation/deactivation kinetics. In contrast, $I_{K,s}$ is insensitive to E-4031, has an approximately linear ion-transfer characteristic, and has slower activation/deactivation kinetics (102, 103).

We have developed models of $I_{K,s}$ and $I_{K,r}$ on the basis of data from rabbit SA and AV nodal cells (49) and

rabbit atrial myocytes (84). $I_{K,r}$ has been described using the general mathematical forms of Shibasaki (104) to model its voltage and time dependence (Table 5). In contrast to previous models of DiFrancesco and Noble (28) and Rasmusson et al. (98, 99), these expressions include a fast inactivation variable (p_i) in the description of its gating. The inclusion of p_i produces inward rectification in the fully activated ion transfer ($I-V$) curve (Fig. 7C), thus attenuating the role of $I_{K,r}$ at more depolarized potentials. Moreover, the rapid reactivation kinetics of p_i generate a transient increase in outward current during a tail current voltage-clamp protocol (not shown) (111).

The $I_{K,r}$ and $I_{K,s}$ models are shown in Fig. 7. Figure 7B illustrates the steady-state gating model (\bar{n}) for the slowly activating $I_{K,s}$. As illustrated in Fig. 7A, the steady-state activation (\bar{p}_a) curve for $I_{K,r}$ measured using whole cell methods by Habuchi et al. [$V_{1/2} = -14.6$ mV, slope factor (k) = 6.9 mV] (49) is in good agreement with the single channel-derived measurement of Veldkamp et al. ($V_{1/2} = -7.3$ mV, k = 7.7 mV) (111) and the whole cell measurement of Muraki et al. ($V_{1/2} = -14.1$ mV, k = 5.7 mV) (84). However, it differs by +10 to +20 mV from Shibasaki's data ($V_{1/2} = -25.1$ mV, k = 7.4 mV) (104). To determine the steady-state parameters associated with p_i , we adopted the rapid Shibasaki inactivation kinetics and used least squares parameter estima-

tion (79) to produce appropriate inward rectification for $I_{K,r}$. Figure 7C illustrates the simulated $I-V$ curve for $I_{K,r}$, which is consistent with data from rabbit atrial (84) and rabbit SA and AV nodal (Y. Habuchi and W. R. Giles, unpublished data) myocytes. Unfortunately, attempts to quantify the voltage-dependent activation kinetics of $I_{K,r}$ and $I_{K,s}$ proved unsatisfactory; consequently, τ_{p_a} and τ_n were modeled in qualitative terms. The resultant voltage dependence of τ_{p_a} is comparable in peak magnitude to guinea pig atrial measurements by Sanguinetti and Jurkiewicz (103) but generates somewhat more rapid deactivation at diastolic membrane potentials.

The studies of Muraki et al. (84) in rabbit atrial cells at 34°C have suggested that $I_{K,r}$ provides the major delayed rectifier current in rabbit atrial myocytes. In our simulations, however, we have found that fast and slow currents are required to adequately model the rabbit atrial action potential. In particular, $I_{K,s}$ is required to supply the necessary outward current to initiate early repolarization; $I_{K,r}$ proves inadequate for this task because of its strong inward rectification.

Inward Rectifier

The inward rectifier (I_{K1}) supplies a functionally important K^+ current in most cardiac cells. I_{K1} helps

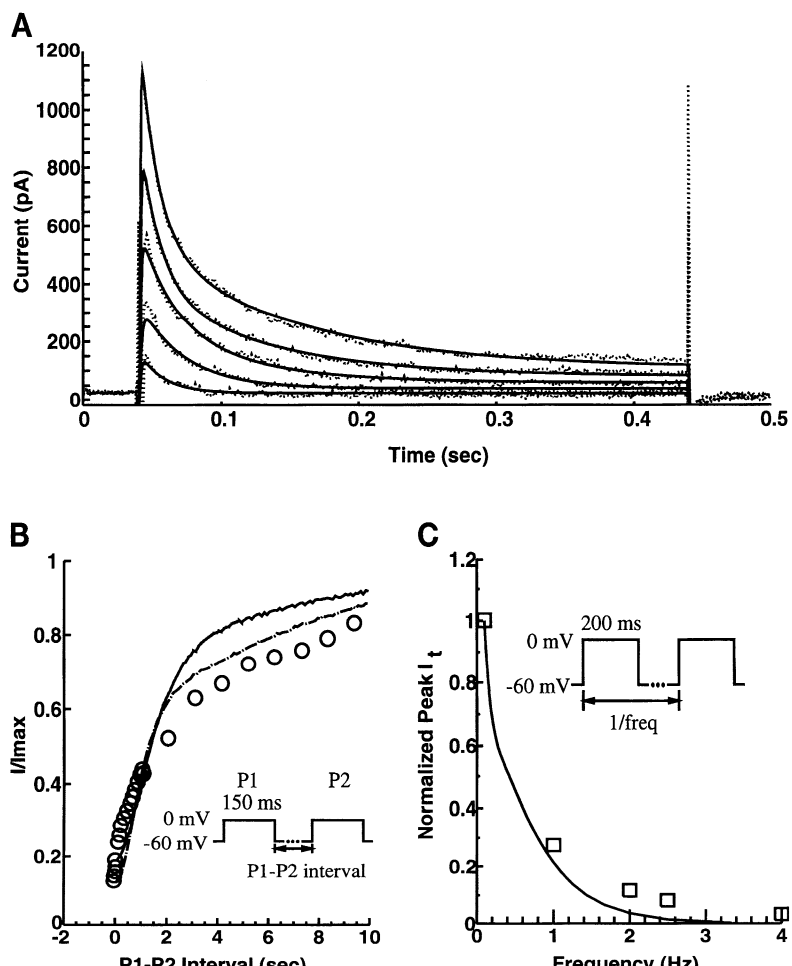


Fig. 6. Voltage-clamp measurements of transient outward current. A: 5 superimposed experimental records (points) and model-generated fits (solid curves) to time-dependent transient outward current recorded by Fedida and Giles in 35°C ventricular epicardium (Fig. 6a in Ref. 35). Protocol consisted of 400-ms depolarizing steps to -20, -10, 0, 10, and 20 mV applied at 10-s intervals. Each outward current is modeled as sum of I_t and $I_{B,Cl}$. B: a double-pulse protocol (inset) probes reactivation time course of measured (○) and model-generated (solid curve, 30°C; dashed-dotted curve, 35°C) I_t responses. Current evoked during pulse P2, normalized to that during pulse P1, is shown as a function of interpulse interval. P2/P1 ratio measures changes in I_t availability (s_{total}) with time. In all traces, longer interpulse intervals lead to a more fully reactivated I_t (higher s_{total}). C: frequency dependence of peak I_t evoked in steady state from a train of voltage-clamp steps (inset) normalized to peak current under a 0.1-Hz step frequency. Model-generated (solid curve, adjusted to 36°C) and recorded (□, 36°C) (Fig. 2C in Ref. 38) rabbit atrial responses are shown.

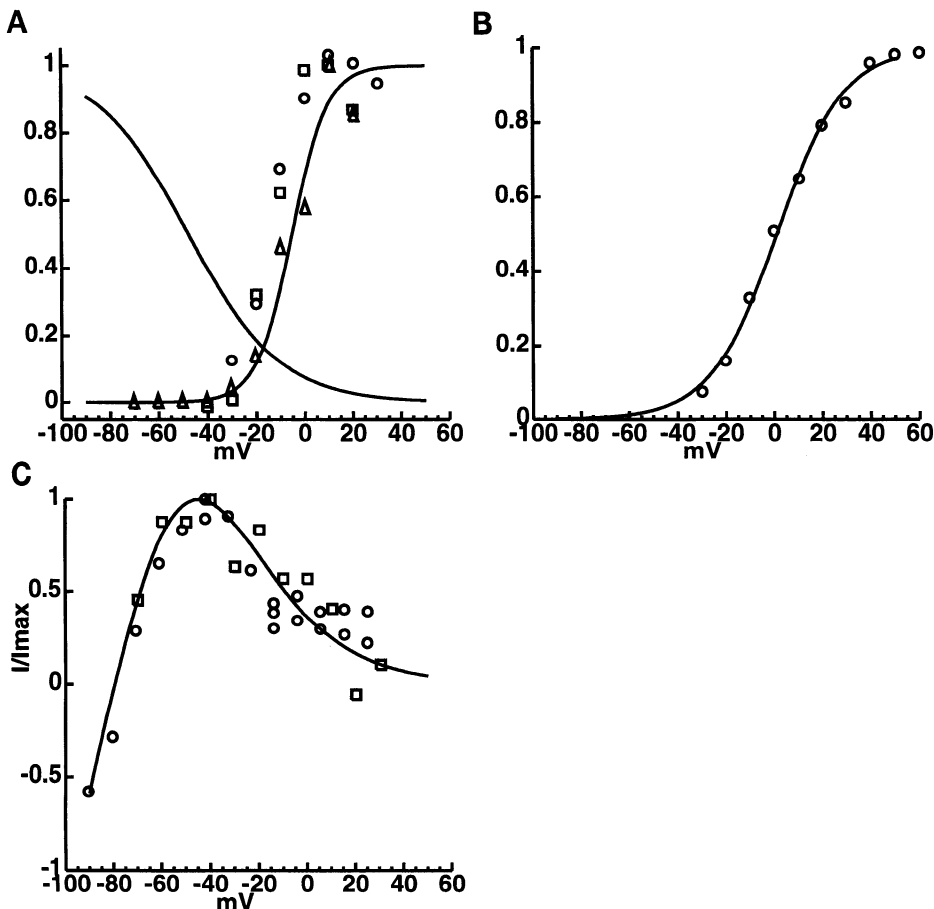


Fig. 7. Parameters describing fast and slow delayed rectifier K^+ currents. A: steady-state activation (\bar{p}_a , right) and inactivation (\bar{p}_i , left) curves for I_{K_r} . Data are from Habuchi et al. (○) (Fig. 3B in Ref. 49), Veldkamp et al. (Δ) (Fig. 8 in Ref. 111) and Muraki et al. (□) (Fig. 1Ab in Ref. 84). B: steady-state activation (\bar{n}) curve for I_{K_s} . Data are from Habuchi et al. (○) (Fig. 3B in Ref. 49). C: model-generated fully activated I - V relation for I_{K_r} normalized to maximum outward current. Data are from Muraki et al. (□) (Fig. 2Ab in Ref. 84) from rabbit atrial myocytes. Similar results (○) have been obtained in rabbit SA and AV nodal cells (Y. Habuchi and W. R. Giles, unpublished data).

establish the RP and input resistance (R_{in}) of the quiescent cell. In addition, I_{K1} contributes to the action potential by supplying outward current during late repolarization. These roles arise from the strong inward rectification of its I - V relation (Fig. 8) and its dependence on extracellular K^+ concentration ($[K^+]_o$). The I_{K1} - V relationship at the resting potential (nominally $V = -71.0$ mV) reveals an outward current and

ward rectification of its I - V relation (Fig. 8) and its dependence on extracellular K^+ concentration ($[K^+]_o$). The I_{K1} - V relationship at the resting potential (nominally $V = -71.0$ mV) reveals an outward current and

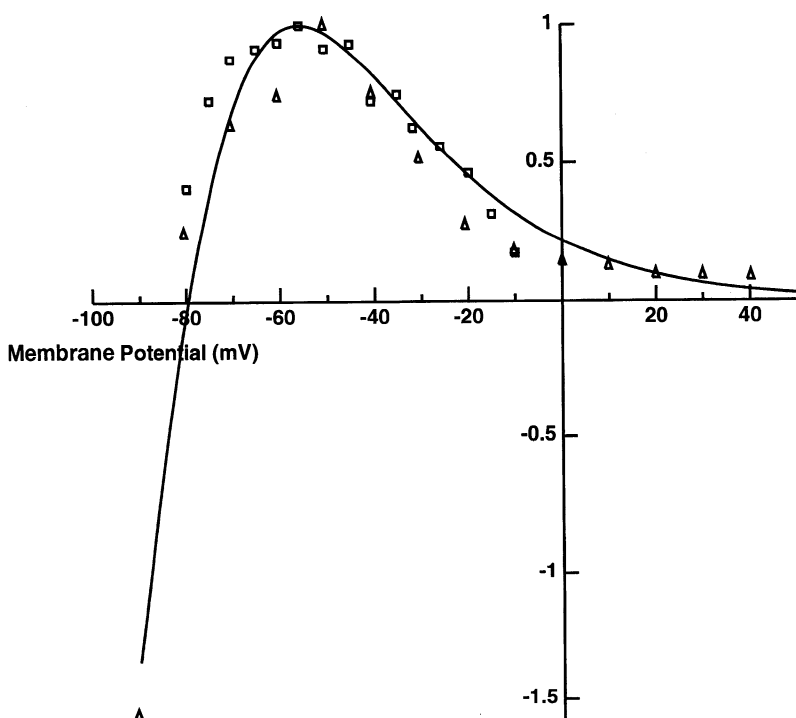


Fig. 8. Normalized I - V relations for inward rectifier K^+ current. Currents have been normalized for maximum outward current occurring near V of -60 mV [typically ~30 pA in rabbit atrial and 200 pA in rabbit ventricular cells (46, 107)]. I - V curves are shown for model (solid curve) rabbit ventricular myocytes (Δ) (Fig. 11D in Ref. 45), and rabbit atrial myocytes (□) [Fig. 7B (inset) in Ref. 84].

positive slope conductance. This outward current helps balance resting inward leakage currents, and the large slope strongly influences cell conductance in the quiescent state.

Experimental studies by Giles and colleagues (45, 84, 107) have identified I_{K1} in rabbit atrial and ventricular cells and have demonstrated a modulatory effect of $[K^+]_o$. However, the size of I_{K1} in the atrium, measured as the Ba^{2+} -sensitive (100 μM) current, is 5 (84, 107) to 10 (46) times smaller than in the ventricle. In rabbit atrial cells at 34°C, an average peak outward current of 36 pA was measured using triangular voltage-clamp command waveforms to approximate the action potential (84).

Figure 8 shows the normalized I_{K1} -V relation of the model together with data from rabbit ventricular (107) and atrial (84) preparations. Shimon et al. (107) reported the gating associated with I_{K1} to be relatively rapid. Consequently, we have treated the inward rectifier as an instantaneous current in our model. The equation utilized for I_{K1} (Table 6) also provides an empirical representation of the modulation of I_{K1} by $[K^+]_o$ (107) and allows our model to adequately fit the terminal (final) phase of repolarization.

Ca^{2+} -Activated K^+ and Cl^- Currents

A combination of Ca^{2+} -activated K^+ and Cl^- currents ($I_{K,Ca}$ and $I_{Cl,Ca}$) produces a 4-AP-insensitive transient outward current that is thought to accompany the $[Ca^{2+}]_i$ transient and the action potential. $I_{K,Ca}$ has been described in rabbit ventricular and atrial myocytes by Hiraoka and Kawano (58), Giles and Imaizumi (45), and Zygmunt and Gibbons (115, 116). In rabbit atrial myocytes, $I_{K,Ca}$ has been found to be much smaller than other outward currents (45, 116). Zygmunt and Gibbons (116) also described a Ca^{2+} -induced Cl^- current. Unfortunately, the available data do not provide a sufficient basis to model $I_{Cl,Ca}$ quantitatively. Because $I_{Cl,Ca}$ and $I_{K,Ca}$ are much smaller than I_t (45, 116), we have chosen to neglect these currents in our model.

Na^+/Ca^{2+} Exchanger

The Na^+/Ca^{2+} exchanger couples the electrical and Ca^{2+} transport functions of the sarcolemmal membrane. Whereas the current carried by the Na^+/Ca^{2+} exchanger is usually small compared with channel-mediated ionic currents, I_{NaCa} may influence APW under conditions where $[Ca^{2+}]_i$ is high, repolarization velocity (an indicator of net membrane current) is low, or membrane potential is hyperpolarized. Na^+/Ca^{2+} exchange also provides a significant pathway for extrusion of Ca^{2+} from the myoplasm. At rest, Na^+/Ca^{2+} exchange transports relatively little Ca^{2+} because of low $[Ca^{2+}]_i$ levels and the low Ca^{2+} -binding affinity of the Na^+/Ca^{2+} exchanger compared with the sarcolemmal Ca^{2+} pump (I_{CaP}). However, when I_{NaCa} is enhanced by high $[Ca^{2+}]_i$ or negative potentials, Ca^{2+} removal from the intracellular medium via I_{NaCa} may greatly exceed that via I_{CaP} (16).

A simplified form of the Mullins (83) expression for I_{NaCa} , which has been used in the DN model (28) and in

our previous studies on bullfrog (98, 99) and rabbit ventricular (45) myocytes, is also used in this rabbit atrial cell model. When a 3:1 stoichiometry is assumed, the exchanger reversal potential, as measured by Kimura et al. (67), is in close agreement with the estimated value for the reversal potential given by $E_{NaCa} = (n_{NaCa}E_{Na} - 2E_{Ca})/(n_{NaCa} - 2)$, where n_{NaCa} is the stoichiometry. In addition, Kimura et al. reported Hill coefficient values for the dependence of I_{NaCa} on extracellular Na^+ and Ca^{2+} of 2.9 and 0.9, respectively, suggesting that a stoichiometry of 3 Na^+ :1 Ca^{2+} is appropriate. Noble (90) introduced a partition parameter, γ , from Eyring rate theory, which determines the symmetry between the voltage dependence of outward and inward fluxes of the exchanger. A value of 0.5 specifies symmetrical voltage dependence of the inward and outward fluxes about the reversal potential. Earm and Noble (31) and Kimura et al. suggested that this value is <0.5, because the inward and outward components of the I_{NaCa} -V curve are not symmetrical. We have used a nonlinear least squares parameter estimation method (79) to fit the general form of the I_{NaCa} equation (Table 10) to experimental data of Earm and Noble from single rabbit atrial cells. In applying the method, we have fixed the stoichiometry of I_{NaCa} at the value used by Earm and Noble and Kimura et al. ($n_{NaCa} = 3$). Least squares estimates for two parameter values, k_{NaCa} and γ , were then obtained for various values of d_{NaCa} and $[Ca^{2+}]_i$ until an acceptable representation was achieved. In particular, because Earm and Noble measured I_{NaCa} as a Ca^{2+} -sensitive difference current, an attempt was made to utilize a physiologically realistic value of $[Ca^{2+}]_i$ in the fit. The resulting "fully activated" I_{NaCa} -V curve (Fig. 9) was obtained using $[Ca^{2+}]_i$ of 2 μM , d_{NaCa} of 0.0003, k_{NaCa} of 0.141, and γ of 0.470. However, in our action potential simulations, we have modified k_{NaCa} and γ to 0.016 and 0.45, respectively.

Na^+-K^+ Pump

The Na^+-K^+ pump current (I_{NaK}) utilizes energy derived from ATP to maintain Na^+ and K^+ electrochemical gradients across the sarcolemma. This current has been described in detail in guinea pig ventricle (19, 42, 85) and has also been studied in bullfrog atrium (105). The detailed models of Chapman et al. (19) and Lemieux et al. (71) account for the dependence of pump activity on $[Na^+]_i$, $[K^+]_o$, adenosine triphosphatase activity, membrane potential, and time. We have adopted a less sophisticated model that treats I_{NaK} as an instantaneous function of $[Na^+]_i$, $[K^+]_o$, and V (see Table 9). In this expression, the voltage-dependent term mimics the data of Gadsby and Nakao (42) from guinea pig ventricular myocytes at 36°C. The voltage-dependent term is a hyperbolic function scaled to match the relative changes in I_{NaK} as a function of membrane potential (cf. Ref. 41). Concentration-dependent terms are based on Michaelis-Menten models. Activation of the pump by extracellular K^+ is described using a Hill coefficient of 1 (23, 43) and a nominal K_{m,K_o} of 1.0 mM. The K_m value was chosen to be intermediate between that reported by Cohen et al.

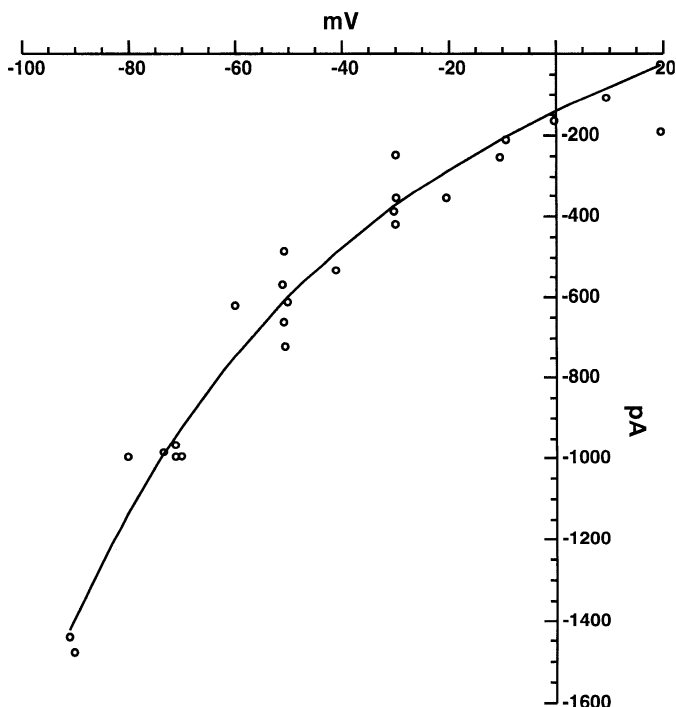


Fig. 9. I - V relation for $\text{Na}^+/\text{Ca}^{2+}$ exchanger assuming high ($2 \mu\text{M}$) $[\text{Ca}^{2+}]_i$. Model fit (solid curve) to data (○) of Earm et al. (Fig. 10 in Ref. 30) from single rabbit atrial cells is shown. Model parameter values are as follows: $n_{\text{NaCa}} = 3$, $[\text{Ca}^{2+}]_i = 2 \mu\text{M}$, $d_{\text{NaCa}} = 0.0003$, $k_{\text{NaCa}} = 0.141$, $\gamma = 0.470$.

(23) (0.8 mM) and that reported by Gadsby and Nakao (43) (1.4 mM). Activation of I_{NaK} by intracellular Na^+ is described using a Hill coefficient of 1.5, in agreement with Gadsby and Nakao (43) ($n_H \sim 1.4$), and a K_{m,Na_i} of 11 mM (43). The ratio of Hill coefficients reflects the well-known 3:2 stoichiometry of the Na^+/K^+ pump (32). The expression used for I_{NaK} in the present study is similar to that used by Luo and Rudy (76). In contrast, the expression for I_{NaK} (or i_p) in DiFrancesco and Noble (28) assumed a 1:1 stoichiometry for Na^+/K^+ coupling and did not include voltage dependence.

In modeling the rabbit atrial action potential, we have adjusted the maximum transport capacity (I_{NaK}) of the Na^+/K^+ pump to reflect current densities measured in isolated cardiac myocytes. In our model, I_{NaK} supplies 12–22 pA or 0.24–0.45 pA/pF of outward current over the range of atrial membrane potentials. Comparable ouabain-sensitive current densities of I_{NaK} have been measured in rabbit ventricular cells: 15–20 pA (W. R. Giles, personal communication) and 0.32 pA/pF (61).

The $[\text{Na}^+]_i$ and V dependence of I_{NaK} (Table 9) suggests that different $[\text{Na}^+]_i$ levels are appropriate for the quiescent and actively stimulated cell. In our model, membrane current balances have been adjusted, such that a true resting condition occurs when $[\text{Na}^+]_i$ is 6.6 mM and V is -71.7 mV . In the actively stimulated cell, the magnitude of I_{NaK} is sufficient to approximately balance inward Na^+ fluxes through membrane channels when $[\text{Na}^+]_i$ equals the average values reported by Désilets and Baumgarten (8.4 mM) (27) from ion-sensitive electrode recordings. For example, cycle-to-

cycle variation in $[\text{Na}^+]_i$ is minimal ($<5 \mu\text{M}/\text{s}$) during model simulations at 2.0 Hz. However, cessation of stimulation leads to a slow decrease in $[\text{Na}^+]_i$ (roughly $18 \mu\text{M}/\text{s}$) and slow membrane hyperpolarization toward the resting state, inasmuch as the absence of action potentials allows I_{NaK} to effect a net extrusion of Na^+ .

Ca^{2+} Pump

The Ca^{2+} pump (I_{CaP}) is a low-capacity high-affinity transport mechanism that helps maintain the low resting level of $[\text{Ca}^{2+}]_i$. In noncardiac tissues, studies by Niggli et al. (87) suggest that Ca^{2+} transport is mediated by $\text{Ca}^{2+}/\text{H}^+$ exchange. This is also a possibility in mammalian heart, where such exchange might be considered within a detailed model of intracellular H^+ homeostasis. For simplicity, we have chosen to ignore the role of H^+ and to employ the electrogenic formulation for I_{CaP} used in our previous studies (98) and shown in Table 8. Although I_{CaP} is considered essential for Ca^{2+} homeostasis, the electrogenic model provides only a very small outward contribution ($\sim 5 \text{ pA}$) to the total background current of the myocyte. This pump is not considered in the DN model (28), whereas a nonelectrogenic formulation was employed in the HN model (56).

INTRACELLULAR MEDIUM

Myocyte Ultrastructure

We have utilized experimental data to provide accurate values of model parameters related to the ultrastructural geometry of the rabbit atrial myocyte. Structurally, the myocyte was assumed to have an idealized cylindrical geometry, and specifications of cell diameter (11 μm), length (130 μm), volume, surface area, and capacitance were obtained from average values reported by Giles and Imaizumi (46). The total intracellular volume (Vol_i) was calculated from these specifications, and subcellular volumes were determined as fractions of Vol_i on the basis of the ultrastructural analysis of Page (Table 3 in Ref. 95) in rat left ventricular myocardium. These included the myofibrillar volume (Vol_{Ca} , 46.7% of Vol_i), the terminal cisternal SR volume (Vol_{rel} , 0.0035% of Vol_i), and the noncisternal SR volume (Vol_{up} , 0.0315% of Vol_i) (95). These volumes were utilized in the material balance equations for Na^+ , K^+ , and Ca^{2+} (Tables 11 and 13). In particular, Na^+ and K^+ are assumed to diffuse freely throughout the cytosolic volume (Vol_i). In contrast, Ca^{2+} was considered to be localized in discrete cellular compartments. Two of these (corresponding to Vol_{up} and Vol_{rel}) were used to model the handling of Ca^{2+} by the SR. Mitochondrial transport of Ca^{2+} has been determined to be slower and under physiological conditions much less significant than that mediated by the SR and sarcolemma (1). Consequently, the mitochondrial volume, as well as other (e.g., nuclear) volumes, was modeled as impermeable to Ca^{2+} , and the corresponding Ca^{2+} fluxes were considered to be zero. The remaining cytosolic volume, that of the myofibrils (Vol_{Ca}), provided the “common pool” (109) compartment for the material balance of free intracellular Ca^{2+} (Table 11).

Ionic Composition

Intracellular concentrations of Na^+ and K^+ were based on the average activities measured by Désilets and Baumgarten (27) using ion-sensitive microelectrodes. Model equations describing the mass balance of these ions are given in Table 11.

Ca^{2+} Buffering

The rate constants for Ca^{2+} binding to calmodulin and troponin were taken from Robertson et al. (100), modified for troponin according to Potter and Zott (97), and scaled from 23 to 35°C by use of a Q_{10} of 1.8. Specifically, Potter and Zott reported a 10-fold reduction in Ca^{2+} -binding affinity for the Ca^{2+} -specific site on troponin associated with the presence of actin; consequently, we have raised the off rate in our model by 10 times. On and off rates for Ca^{2+} binding to calsequestrin within the SR release compartment were based on the study of Cannell and Allen (15) ($K_d = 800 \mu\text{M}$, $k_{on} = 240 \text{ mM}^{-1} \cdot \text{s}^{-1}$) and adjusted to 35°C via a Q_{10} of 1.6. The concentration of calsequestrin in the release compartment of the SR (31 mM) is also taken from Cannell and Allen and derives from the data of MacLennan and Wong (78). Tables 11 and 12 give the model equations governing the buffering and mass balance of intracellular Ca^{2+} .

Sarcoplasmic Reticulum

The mathematical description of the uptake and release of Ca^{2+} by the SR is similar to that used by Hilgemann and Noble (56) and Earm and Noble (31). However, there are several important differences between the HN formulation (56) and our mathematical description of the SR. These differences are as follows.

1) We have used measurements of the Ca^{2+} uptake and release compartment volumes of the SR by Page (95). Page reports that the Ca^{2+} release compartment is 10 times smaller than the Ca^{2+} uptake compartment, whereas the reverse holds in the HN model.

2) The HN model assumes that cytosolic Ca^{2+} buffers are in steady state, whereas our model includes simulations of the dynamics of these buffers (100). The time constant for changes in the occupancy by Ca^{2+} on the Ca^{2+} -specific site of troponin varies between 5.1 ms when $[\text{Ca}^{2+}]_i$ is 50 nM and 4.3 ms when $[\text{Ca}^{2+}]_i$ is 1.0 μM during the action potential. The assumption that this buffer is in steady state during the action potential is not valid.

3) We have included calsequestrin in the Ca^{2+} release compartment of the SR as an essential and very substantial Ca^{2+} buffer.

4) To prevent CICR at the resting potential (-71.0 mV) and resting Ca^{2+} concentration (50.0 nM), we have increased the Hill coefficient for Ca^{2+} binding to the sarcoplasmic Ca^{2+} release channel from 2 to 4. This increase reduces the sensitivity to Ca^{2+} at concentrations $<0.1 \mu\text{M}$ while maintaining it at concentrations $>0.5 \mu\text{M}$.

5) We have modified several parameters associated with size and kinetics of SR uptake and release cur-

rents to give an appropriately triggered release of Ca^{2+} in response to influx through high-threshold Ca^{2+} channels ($I_{\text{Ca,L}}$). The parameters in question include the Ca^{2+} -binding affinity of the release gate (lowered from 500 to 300 μM), the maximum uptake and release currents, and the scaling of rate constants associated with the three-state release gate mechanism.

In our adaptation of the HN model, SR Ca^{2+} release is triggered primarily by $[\text{Ca}^{2+}]_i$ (i.e., CICR). A term dependent on membrane potential is also present to qualitatively model the "local control" (113) of CICR under conditions in which $I_{\text{Ca,L}}$ is small but Ca^{2+} release should still occur. This is discussed briefly by Hilgemann and Noble (56). The voltage-dependent contribution to the activation of SR release is normally much smaller than the Ca^{2+} -dependent term.

Table 13 provides the equations used to describe SR Ca^{2+} handling and Ca^{2+} buffering by calsequestrin in the release compartment of the SR.

MODEL PARAMETERS

Assignment of Parameter Values

Several criteria have been used to assign values to the model parameters of this study. The majority of model parameter values shown in Tables 2–14 have been determined from biophysical (e.g., voltage-clamp) studies of isolated model elements (e.g., ionic currents), as discussed above. In general, when whole cell responses have been examined, these values were considered fixed and characteristic of the nominal rabbit atrial myocyte. A second category of model parameters has been employed to adjust those equations derived from biophysical measurements made under nonphysiological conditions to a more physiological state. This includes parameters such as Q_{10} factors used to scale the kinetics of ionic currents from a reduced temperature (e.g., 17°C for I_{Na}) to the physiological value of 35°C. In the absence of constraining data, these assignments have been made on a qualitative basis. A third group of parameters, the values of which have not been determined from "primary data" (e.g., voltage-clamp studies), have been adjusted to mimic "secondary data" (e.g., action potentials). This includes the maximal whole cell conductance parameters associated with ionic currents, pumps, and exchangers. Voltage-clamp experiments that provided steady-state and/or kinetic data for a particular ionic current may have limited use in determining a current density or, equivalently, a maximal whole cell conductance appropriate for action potential simulations. In some cases, the voltage-clamp data originated from a different cardiac cell type than from rabbit heart; moreover, action potential and voltage-clamp data for a particular cell type were almost always obtained from different cells. Therefore, ionic conductances were treated as free parameters when the model was adjusted to mimic integrated properties of the atrial myocyte and to simulate action potentials. As discussed below, some of these conductances have been constrained to mimic the passive electrophysiological characteristics of the quiescent cell. We have at-

tempted to minimize those adjustments to model parameters in the simulation of action potentials, particularly if this caused deviation from the data described previously. However, in rare cases, small modifications (e.g., to τ_{p_a} , a parameter based on primary data) proved necessary for adequate action potential mimicry.

The parameter values used in this study have been adjusted to fit within a larger context with regard to rate variability of the rabbit atrial action potential. The model-generated responses presented below result from simulations using a single set of parameter values given in Tables 2–14.

Parameter Constraints for the Quiescent Myocyte

Unlike pacing cells, healthy enzymatically isolated atrial myocytes are electrically and mechanically silent and must be stimulated to evoke action potentials. This “background” or “resting state” is determined by the passive electrical characteristics of the resting cell membrane, as well as the steady-state transcellular distribution of permeant ions. Very accurate mathematical representation of the background state is a prerequisite for valid modeling of the action potential. Membrane currents that contribute to the resting state (i.e., I_{K1} , $I_{B,Na}$, $I_{B,Ca}$, $I_{B,Cl}$, I_{NaK} , I_{NaCa} , and I_{CaP}) influence all phases of the action potential. The relative sizes of background currents are specific to the cardiac cell type, because passive electrical characteristics of the sarcolemma differ with cell type in heart (46). For a true resting condition, the sizes of background currents must provide for appropriate equilibria with respect to transsarcolemmal transport and the intracellular milieu.

In our model, in the resting state, 1) membrane potential is stable at the RP, 2) R_{in} measured at the resting state is $\sim 600\text{ M}\Omega$, 3) the net Ca^{2+} flux across the sarcolemma is zero, and 4) the net Na^+ flux across the sarcolemma is zero. The sizes of background currents (conductances and maximum transport capacities; Table 14) have been adjusted to satisfy these constraints at an assumed resting state ($[\text{Na}^+]_i = 6.6\text{ mM}$, $[\text{Ca}^{2+}]_i = 50.0\text{ nM}$, membrane potential = -71.0 mV). Consequently, acceptable membrane properties and ionic stability have been achieved simultaneously.

Table 16 compares C_m , RP, and R_{in} of the model atrial cell with experimental values. C_m and RP represent nominal values for a typical atrial myocyte (50 pF and -71 mV), and R_{in} falls within the range given by Giles and Imaizumi (46). Model R_{in} has a strong dependence on the sizes of the background currents and, in particular, I_{K1} , a consequence of the slope of the inward rectifier ion transfer (I-V) characteristic near E_K .

Acceptable balances of ionic fluxes have been achieved by selecting a lower $[\text{Na}^+]_i$ level in the resting than in the working state. In the assumed resting condition, $[\text{Na}^+]_i$ lies below the value (8.4 mM) measured by Désilets and Baumgarten (27), and the model achieves a true equilibrium with no net transsarcolemmal Na^+ or Ca^{2+} flux. When the cell is stimulated at 2.0 Hz from the nominal initial state (Table 15), where $[\text{Na}^+]_i$ is 8.4 mM, the total Na^+ load is approximately balanced by

I_{NaK} over each pacing cycle. However, when pacing is terminated, a small slow downward drift in $[\text{Na}^+]_i$ and membrane potential results.

RESULTS

We have quite extensively tested whether our model can simulate integrated whole cell properties and fundamental electrophysiological responses in rabbit atrium. Simulated responses have been compared directly with experimental measurements from enzymatically isolated rabbit atrial myocytes. To the extent that these agree, we are justified in using the model to assess contributions of functionally important components to whole cell electrophysiological behavior.

Simulated APW

Figure 10A shows the recorded and model-generated action potentials (35°C) at a stimulus rate of 2.0 Hz, which is similar to the pacing rates used in experimental studies. The action potential has a rapid upstroke (*phase 0*), a modest plateau (*phase 2*), and a noticeable increase in repolarization velocity during late repolarization (*phase 3*). The phase of early rapid repolarization (*phase 1*) is not prominent but is present in action potential waveforms at lower stimulus rates (46). The prominence of *phase 1* repolarization has been correlated with the size of I_t (8, 46), suggesting a relatively small role for I_t in this action potential.

Figure 10, B–D illustrates the model-generated membrane currents that underlie the simulated action potential. In Fig. 10A, the action potential upstroke, produced by I_{Na} , has a maximum velocity (\dot{V}_{max}) of 131 V/s and corresponds to a peak I_{Na} of $\sim 6.0\text{ nA}$. Because peak I_{Na} is significantly larger than all other ionic currents, we have not included it in Fig. 10. Figure 10B shows transients for the next two largest ionic currents, I_t and $I_{Ca,L}$. Consistent with the relatively slow rate of early repolarization, the model-generated transient in I_t has a magnitude and time course comparable to $I_{Ca,L}$. Nevertheless, a small *phase 1* repolarization “notch” is evident in model-generated and recorded action potentials. During the plateau phase, I_t and $I_{Ca,L}$ deactivate and delayed K^+ currents ($I_{K,s}$ and $I_{K,r}$) activate, initiating repolarization (Fig. 10C). Although the activation kinetics of $I_{K,s}$ are less rapid than those of $I_{K,r}$, both $I_{K,s}$ and $I_{K,r}$ support the late repolarization phases. The final phase of repolarization is aided by an increase in I_{K1} but is opposed by the increasing inward currents I_{NaCa} and I_B as well as a declining I_{NaK} (Fig. 10, C and D). The size of I_{NaK} is consistent with ouabain-sensitive measurements (see MODEL DEVELOPMENT) and is comparable in magnitude to the outward K^+ currents. Thus I_{NaK} provides a significant repolarizing current throughout this simulated rabbit atrial action potential. Our model is able to mimic the long “tail” that is present in the latest phases of atrial repolarization; it is due to an interaction between the currents contributing to the resting state of the cell (I_{K1} , I_{NaK} , I_{CaP} , I_B , and I_{NaCa}).

Figure 11 presents model-generated Ca^{2+} fluxes and transients within the rabbit atrial model under a

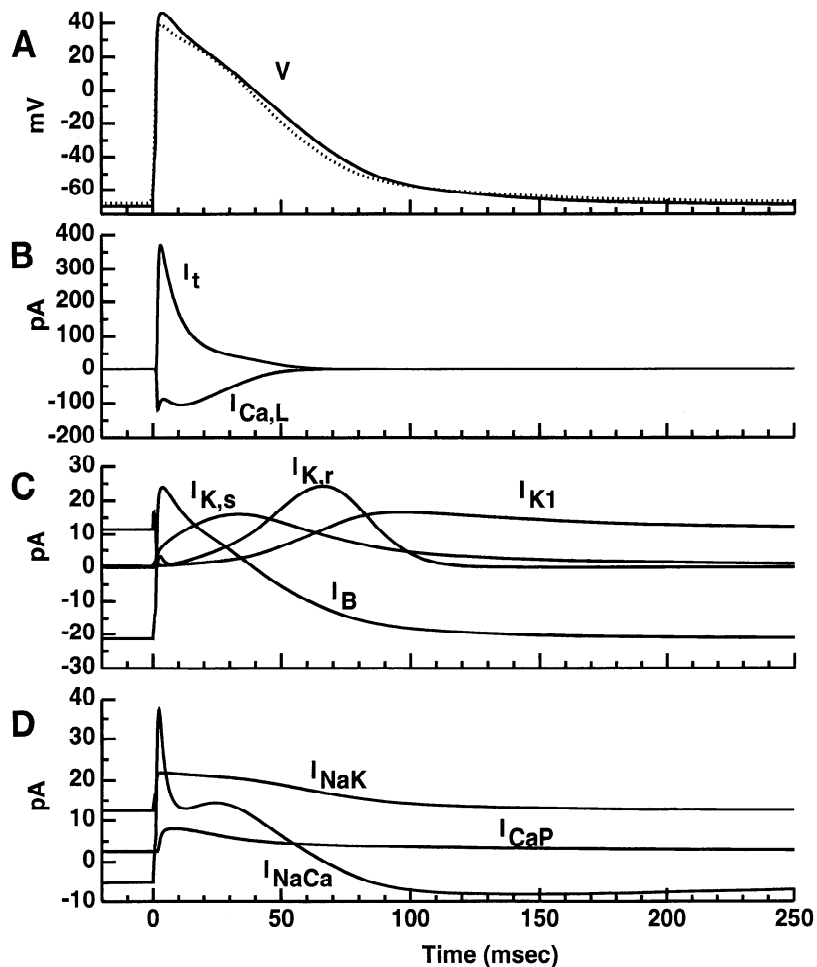


Fig. 10. Simulated and recorded action potentials at 2.0-Hz stimulus rate. *A*: model-generated and recorded action potentials. *B* and *C*: ionic currents. *D*: background pump and exchanger currents. Action potential data in *A* (*dotted line*) was obtained by A. Braun and W. R. Giles (unpublished observations).

2.0-Hz stimulus rate. The predicted $[Ca^{2+}]_i$ transient is shown in Fig. 11B. After the action potential upstroke, free $[Ca^{2+}]_i$ levels rise rapidly from the low diastolic level to a peak. The maximum rate of rise of $[Ca^{2+}]_i$ corresponds temporally to the peak Ca^{2+} release signal from the SR (Fig. 11D). This transient rise in $[Ca^{2+}]_i$ results primarily from SR Ca^{2+} release. The increase in free intracellular Ca^{2+} is considerably smaller than the 65 μM change predicted from the amount of Ca^{2+} released by the SR. This is due primarily to fast Ca^{2+} binding by calmodulin and troponin (Fig. 11C). Sequestration of Ca^{2+} back into the uptake compartment via SR Ca^{2+} pumping (Fig. 11E) also limits peak $[Ca^{2+}]_i$. At this stimulus rate, the SR release compartment retains a portion of its diastolic Ca^{2+} load (Fig. 11F) and calsequestrin buffer sites remain partially occupied throughout the action potential (Fig. 11C). The diastolic interval is sufficiently short in comparison to the SR uptake-to-release transit time to prevent equilibration of Ca^{2+} . Hence, a Ca^{2+} concentration gradient between SR uptake and release compartments exists at all times during the action potential (Fig. 11F).

SR Ca²⁺ Handling

In this model, the SR acts as the most significant supplier and sink of free $[Ca^{2+}]_i$ during the action potential. For example, in Fig. 11, ~93.6% of the Ca^{2+}

load that is released into the intracellular medium during the action potential (systolic phase only) is due to SR Ca^{2+} release. The remaining fractions (4.3, 0.7, and 1.5%, respectively) arise from transmembrane Ca^{2+} influx (via I_{Ca} , $I_{B,Ca}$, and I_{NaCa} , respectively). Membrane currents therefore provide only a small contribution to the $[Ca^{2+}]_i$ transient, in general agreement with the reported dominant role of SR Ca^{2+} release in these cells (2).

Release of Ca^{2+} from the SR is associated with a transient reduction in Ca^{2+} concentration in the release compartment to 30% of its initial value. After the systolic Ca^{2+} release, $[Ca^{2+}]_i$ is restored to low levels through a combination of uptake by the SR and extrusion via the Ca^{2+} pump and Na^+/Ca^{2+} exchanger. The amount of Ca^{2+} removed by the SR uptake mechanism balances the previous SR release load. Transsarcolemmal Ca^{2+} extrusion via I_{NaCa} and I_{CaP} balances the preceding transmembrane Ca^{2+} influx, such that ~73% of the extrusion flux results from Na^+/Ca^{2+} exchange.

Instantaneous I-V Trajectories

When the cardiac action potential is simulated, it is essential to ensure that the model adequately represents not only the APW but also the underlying current densities and transients in membrane currents that generate the action potential. Under space-clamp as-

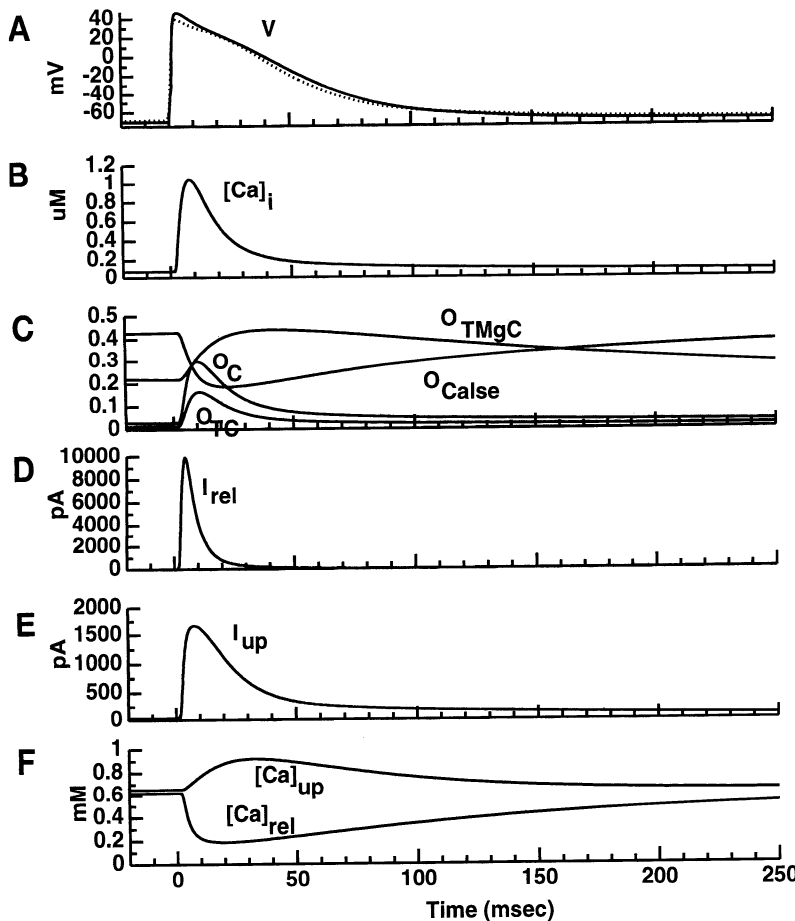


Fig. 11. Model-simulated action potential at 2.0-Hz stimulus rate. A: model-generated and recorded action potentials. B: [Ca²⁺]_i transient. C: Ca²⁺ buffer occupancies for calmodulin (O_C) and Ca²⁺-specific (O_{TC}) and competitive (O_{TMgC}) sites on troponin and calsequestrin (O_{Calse}). D: SR release current. E: SR uptake current. F: transients in Ca²⁺ concentration in SR release ([Ca²⁺]_{rel}) and uptake ([Ca²⁺]_{up}) compartments. Action potential data (dotted line) was obtained by A. Braun and W. R. Giles (unpublished observations).

sumptions, I_{net} is proportional to the time derivative (\dot{V}) of membrane potential (Eq. 1). Because \dot{V} may be calculated from the action potential, the temporal behavior of I_{net} may be determined for the data and the model. Examination of this behavior in the I_{net} - V plane allows the voltage dependence of the model-generated I_{net} and its components to be compared with that derived from the data (I_{data}). We have found this technique to be especially beneficial in obtaining an accurate simulation of action potential data (26).

Figure 12 illustrates the model-generated and experimentally derived I_{net} - V trajectories for the 2.0-Hz action potential, as well as some underlying I - V trajectories of specific membrane currents. In Fig. 12, time is implicit and increases from right to left. For convenience, we have illustrated only the repolarization phases. Therefore, I_{net} is outward, and as time proceeds from right to left I_{net} increases and declines in correspondence with slope changes in the action potential as viewed in the time domain (Fig. 10A).

Figure 12A suggests that early repolarization is "shaped" by I_{Na} and I_t and, to a lesser extent, by $I_{Ca,L}$. At peak overshoot, inactivation has reduced I_{Na} from its peak value (not shown) to a size comparable to I_t and $I_{Ca,L}$. The "spike" of outward current during early repolarization results from the faster decline of I_{Na} than I_t , whereas the local minimum or notch follows from the activation of inward $I_{Ca,L}$ while outward I_t is inactivating. The participation of other currents is illustrated in

Fig. 12B, which shows that 1) I_{NaK} provides an outward current throughout repolarization, 2) $I_{K,s}$ contributes most significantly near +10 mV, and 3) $I_{K,r}$ is recruited maximally near -35 mV. Final repolarization results from the combined effect of I_{K1} and I_{NaK} in opposition to I_{NaCa} and I_B . The maximal amplitudes of I_{K1} and I_K ($=I_{K,r}+I_{K,s}$) during repolarization are predicted to be comparable, in agreement with the rabbit atrial data of Muraki et al. (84). Overall, the I - V trajectories predicted for K⁺ currents in Fig. 12 are qualitatively similar to those measured using triangular voltage-clamp command waveforms to approximate the action potential (Fig. 7 in Ref. 84).

Rate Dependence of the Action Potential

Studies in several fiber preparations (7–11, 110) as well as in single rabbit atrial cells (46) have documented that the waveshape of a particular rabbit atrial action potential depends strongly on the temporal history of previously evoked action potentials. With steady-state stimulation, this dependence is evident as pronounced alterations in the APW as stimulus rate is varied. The rate-dependent features of the rabbit atrial action potential include the minimum diastolic potential (MDP), the upstroke velocity (V_{max}), the prominence of early repolarization, the extent of a plateau, the speed of final repolarization, and the action potential duration (APD). In particular, at physiological

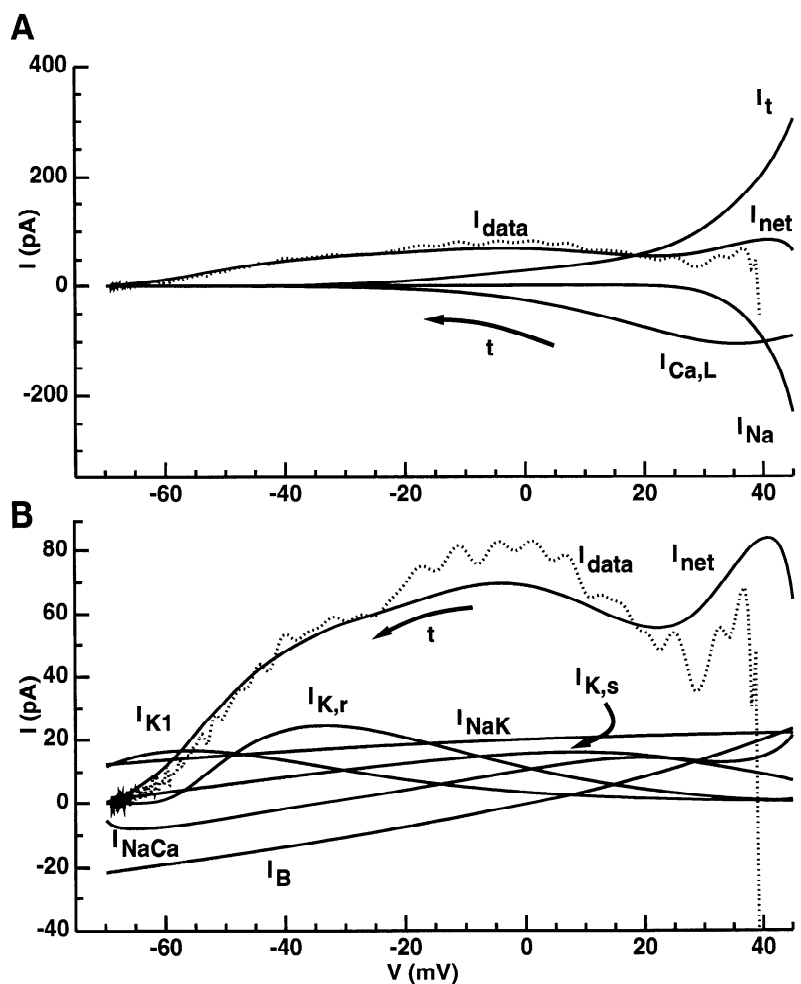


Fig. 12. Model-generated (solid curves) and experimental (dotted curves) instantaneous I - V trajectories during repolarization from peak voltage of action potential (~ -40 mV). Stimulus rate is 2.0 Hz; action potential corresponds to that of Figs. 10 and 11. A: major currents (I_{Na} , I_t , and $I_{Ca,L}$). B: minor and background currents (I_K , I_{K1} , I_{NaCa} , I_{NaK} , and I_B). Trajectories proceed in time from right to left (arrow). Experimental data are from A. Braun and W. R. Giles (unpublished observations).

rates of stimulation, the waveshape has a triangular appearance characteristic of an atrial cell (11). Low stimulus rates or long rest periods are associated with a prominent early repolarization phase (46, 110) that diminishes as rate increases. A substantial I_t has been identified in rabbit atrial cells (46), suggesting a role for I_t in this effect. However, the quantitative roles of I_t and other currents in the rate-dependent variability of the action potential remain only partially defined by experimental data (46).

Figure 13 shows the model-generated and superimposed experimental action potentials for a typical 35°C rabbit atrial myocyte elicited using stimulus frequencies between 0.2 and 3.0 Hz. At high stimulus rates, the action potential has a rapid upstroke, a relatively slow early repolarization phase, a pronounced plateau, and then a more rapid late repolarization phase. As the stimulus frequency is lowered, the APW changes dramatically. Phase 1 of the action potential narrows progressively, and peak overshoot declines. A slowly repolarizing plateau phase develops at negative membrane potentials, giving rise to a "spike-and-dome" appearance to the waveshape at very low frequencies (73). Repolarization is slowed throughout the "middle" phases 2 and 3 of the action potential. Interestingly,

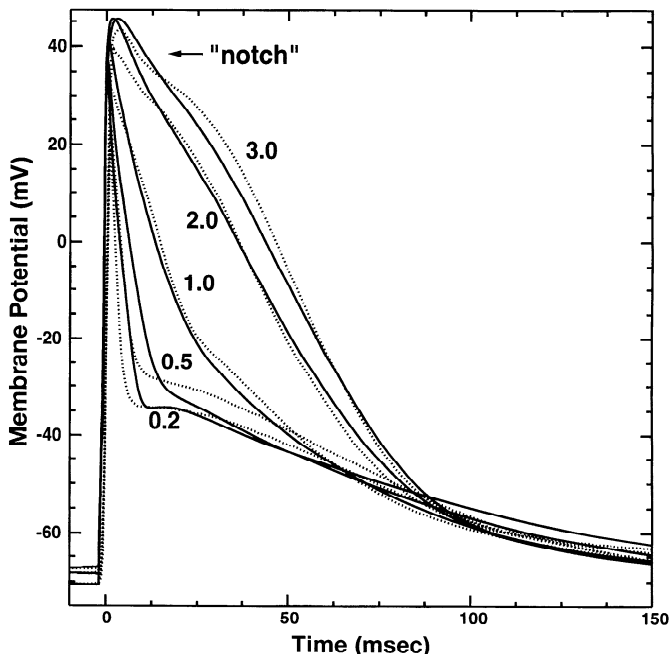


Fig. 13. Simulated (solid curves) and recorded (dotted curves) action potentials at stimulus frequencies of 0.2, 0.5, 1.0, 2.0, and 3.0 Hz. Data are from A. Braun and W. R. Giles (unpublished observations).

however, the final repolarization tail beginning at the end of *phase 3* varies little with rate. The MDP also becomes more hyperpolarized at lower stimulus rates. Although the 3.0- and 0.2-Hz APWs differ significantly, the model closely mimics the major features of each as well as the smooth gradation between waveshapes that occurs over intermediate stimulus rates.

Figure 14 illustrates the model-generated and experimentally derived I_{net} - V trajectories for the 0.2-Hz action potential. Several differences from the 2.0-Hz case (Fig. 12) are displayed prominently in the I - V plane. The model-generated upstroke is somewhat faster at 0.2 Hz than at high rates of stimulation (V_{max} , 152 V/s; peak I_{Na} , 7.3 nA). The increased I_{Na} and V_{max} results from a greater I_{Na} availability (h_{total}) due to a more hyperpolarized MDP. More significantly, I_t provides a much stronger current during early repolarization (Fig. 14A). The long diastolic period allows I_t to recover more completely from inactivation, which leads to an increased magnitude of I_t , a decreased peak overshoot, and a stronger *phase 1* repolarization. This rate dependence of I_t availability is sufficient to simulate the major features of the rate-dependent gradation in early repolarization velocity. The large I_t encountered during *phase 1* is opposed by a sizable slowly inactivating (h_2) component of I_{Na} , so that early repolar-

ization develops from the combined effects of I_{Na} and I_t and, to a lesser extent, $I_{Ca,L}$. A rapid repolarization to a relatively hyperpolarized plateau value near -35 mV deactivates I_t and $I_{Ca,L}$ and allows only minimal activation of delayed rectifier currents ($I_{K,s}$ and $I_{K,r}$). In the latter case, the comparatively longer diastolic interval under a 0.2- than a 2.0-Hz stimulus facilitates a more complete deactivation of $I_{K,s}$ before the upstroke (cf. diastolic currents in Figs. 12B and 14B). Hence, I_K makes only a small contribution to repolarization at 0.2 Hz, and this contribution results primarily from $I_{K,r}$. The primary mediators of the plateau and late repolarization are currents contributing to the resting state of the cell (I_{K1} , I_{NaK} , I_{CaP} , I_B , and I_{NaCa}). Moreover, the termination of the early repolarization phase in Fig. 14A corresponds temporally to a point of high $[Ca^{2+}]_i$ (not shown). This results in a I_{NaCa} more substantial than the earlier high-rate simulation (cf. peak I_{NaCa} in Figs. 12B and 14B). The plateau and late repolarization phases in this case involve a decline in I_{NaCa} coupled with relatively small changes (~ 10 pA) in other background currents. At potentials negative to -55 mV, the net repolarization velocity has little dependence on stimulus rate, and final repolarization is simulated by a balance of rate-independent background currents. As in the 2.0-Hz case, this balance in

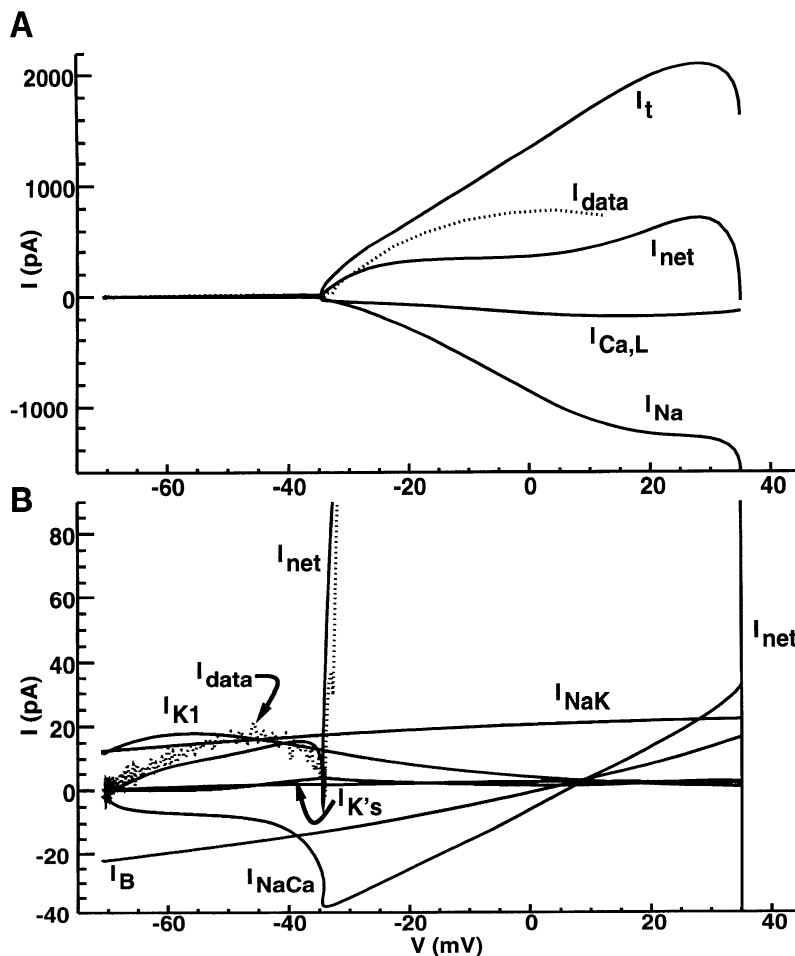


Fig. 14. Stimulation at 0.2 Hz and associated model-generated (solid curves) and experimental (dotted curves) instantaneous I - V trajectories. A: major currents (I_{Na} , I_t , and $I_{Ca,L}$). B: minor and background currents (I_K , I_{K1} , I_{NaCa} , I_{NaK} , and I_B). Trajectories proceed in time from right to left. Data are from A. Braun and W. R. Giles (unpublished observations).

"resting currents" provides excellent mimicry of the long tail in the 0.2-Hz action potential.

In addition to affecting repolarization, stimulus rate can also modify the diastolic and upstroke phases of the action potential. As stimulus rate increases, the shortening of diastole reduces the net Ca^{2+} extrusion occurring via $\text{Na}^+/\text{Ca}^{2+}$ exchange. Consequently, diastolic Ca^{2+} is expected to increase with stimulus rate. This phenomenon is observed within our model (not illustrated). At high stimulus rates, although net $\text{Na}^+/\text{Ca}^{2+}$ exchange is diminished, I_{NaCa} is increased by the raised $[\text{Ca}^{2+}]_i$ levels. This results in more "depolarized" MDP levels at high than at low rates of stimulation.

Refractoriness: Simulated Responses to Premature Stimuli

Normal cardiac tissue undergoes a "refractory period" after the action potential in which the "excitability" or ability to generate a second action potential is transiently reduced (5). The refractory period is divided into "absolute" and "relative" phases. During the former, the tissue is completely inexcitable, whereas stimuli more intense than normal are required to evoke a response during the latter. Excitability then recovers progressively throughout the relative refractory period.

These changes in excitability with time reflect time- and voltage-dependent changes in the gating of membrane currents. Several ionic currents (e.g., I_{Na} , I_t , and $I_{\text{Ca,L}}$) that contribute early in the action potential undergo time- and voltage-dependent inactivation during the action potential and reactivation in diastole. Because our model incorporates appropriate kinetic

information on these currents, it can predict the time course of changes in current "availability" with time.

The major current changes that are responsible for refractoriness can be demonstrated by examining the response to "premature" stimuli. Figure 15 illustrates the model-generated premature stimulus response after steady stimulation (at 2.0 Hz). Figure 15A shows the membrane potential responses to various premature stimuli (5-ms duration, 285-pA amplitude) applied at different times after the initial (periodic) stimulus applied at 0 ms. Figure 15, B and C, illustrates associated transient changes in Na^+ current availability (h_{total}) and the corresponding I_{Na} . Premature stimuli applied earlier than 100 ms fail to invoke an "active" response, and consequently repolarization continues after stimulus termination. Between 100 and 500 ms, a gradually stronger action potential response is elicited as the premature stimulus is delayed. At 500 ms, APW approximately matches the initial "control" response. Consequently, the time interval between 0 and 100 ms corresponds to the "absolute refractory period," and the interval that follows corresponds to the "relative refractory period" in Fig. 15. The recovery of APW to the "control" condition parallels changes in I_{Na} size (Fig. 15C) and availability (Fig. 15B). Consequently, refractoriness in our model is tied directly to I_{Na} reactivation and is resolved via h_{total} into absolute and relative refractory periods.

I_t and $I_{\text{Ca,L}}$ reactivation play a minimal role in this simulation. In the control action potential, I_t helps to define a sharp phase of rapid early repolarization. The combined effects of incomplete reactivation and a re-

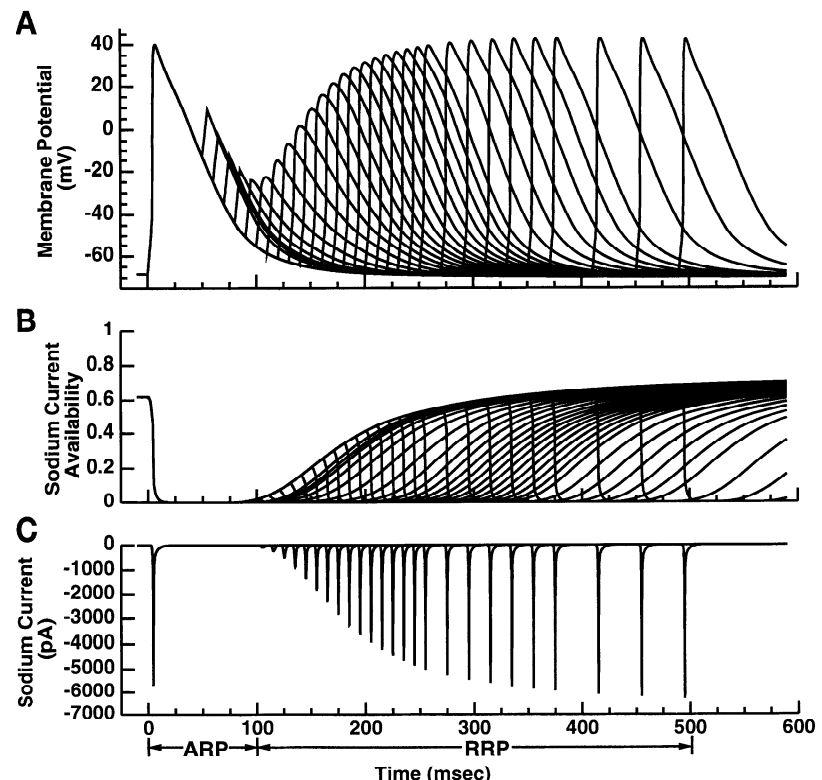


Fig. 15. Measurement of refractoriness after stimulation at 2.0 Hz. Responses to premature stimuli applied at various times after initial stimulus (at 0 ms) are shown. A: membrane potential. B: I_{Na} availability (h_{total}). C: I_{Na} . Predicted absolute and relative refractory periods (ARP and RRP) are labeled below time axis.

duced peak overshoot [limiting ($V - E_K$)] reduces the magnitude of I_t in the premature responses during the relative refractory period. $I_{Ca,L}$ also increases slightly during this period because of more complete reactivation and enhanced activation as the peak overshoot increases. The combined effect of these two currents produces a more rounded peak in the "relative refractory" action potentials than in those elicited by later stimuli.

DISCUSSION

Mathematical modeling constitutes an important adjunct to experimental work in studies of the ionic basis for the cardiac action potential. By use of a reliable quantitative model, the time- and voltage-dependent behavior of membrane currents, resulting concentration changes and buffering, and other cellular events may be studied simultaneously. This enables their integrated effects on the cell to be determined from well-established biophysical principles. Thus action potential models provide useful tools for interpreting and evaluating working hypotheses for observed electrophysiological responses and for predicting the consequences of specific changes on cellular activity. However, the reliability or applicability of model interpretations depends critically on how accurately the model "building blocks" represent their respective cellular components.

We have developed a mathematical model of the rabbit atrial myocyte based extensively on electrophysiological measurements from single enzymatically isolated rabbit atrial cells. As in our previous work (26, 98), we consider the incorporation of biophysical data within a biologically based mathematical framework to be essential in providing a realistic explanation of the behavior and properties of the rabbit atrial cell. Thus, in the process of model development, we have utilized electrophysiological data collected in our laboratory and/or recently published in the literature to characterize the rabbit atrial sarcolemma. In most cases, the data correspond to recordings from isolated cardiac myocytes in rabbit heart, and data from rabbit atrial myocytes have been utilized wherever possible. In addition, we have utilized biochemical and biophysical studies to describe the intracellular milieu. These include measurements of cardiac ultrastructure (95), ionic activity measurements with use of ion-sensitive electrodes (27), and biochemical studies of the important binding kinetics of Ca^{2+} to the buffers troponin and calmodulin within the intracellular medium and calsequestrin within the SR.

In developing this model, we have focused on the descriptions of the membrane currents in the rabbit atrium. Our goal has been to describe the dynamic behavior of these currents as quantitatively as possible. Our model offers a number of improvements over other cardiac cell models (28, 31, 56, 75–77) in the description of the sarcolemmal conductances, including 1) a fast Na^+ current with biexponential inactivation and slow recovery from inactivation; 2) a rapidly activating

transient outward K^+ current with biexponential inactivation, slow reactivation, and appropriate "frequency-dependent" characteristics; 3) two types of Ca^{2+} currents (T and L type), with slow reactivation of the L-type current; 4) two types of delayed rectifier K^+ currents (fast and slow); and 5) background Na^+ , Ca^{2+} , and Cl^- (29) currents.

To ensure an accurate representation of the atrial action potential, our model has been shown to be able to simulate electrophysiological responses under diverse conditions. Voltage-clamp data are simulated for all but the smallest background currents of the model. In one case (I_t), actual current measurements elicited by voltage-clamp depolarization are mimicked closely by model-generated currents over a wide range of membrane voltages. This contrasts with the more common approach of utilizing steady-state activation (inactivation) curve and time constant relationships. In the latter case, these relationships plot only qualitative features of the current transients, such as peak currents and exponential time constant estimates elicited at different clamp potentials. Moreover, the relative contributions of individual currents to the complete model behavior have been constrained to agree with direct (e.g., \bar{I}_{NaK}) or indirect (e.g., \dot{V}_{max}) estimates of their functional size. We have also required that electrophysiological properties resulting from an aggregate of model components (e.g., R_{in}) are consistent with those of isolated rabbit atrial myocytes. In addition, at a physiological rate of stimulation, the model has been shown capable of accurately simulating the nominal rabbit atrial APW in the time and I - V domains.

As a result of this approach, our model can accurately simulate the whole cell voltage-clamp data on which it is based as well as more complex integrated responses (e.g., action potentials) of the atrial myocyte. The model is also able to provide a qualitative prediction of the intracellular Ca^{2+} transient and associated changes in Ca^{2+} buffers and SR Ca^{2+} levels. These predictions are not based on data from our laboratory, but in qualitative terms, the Ca^{2+} load released to the intracellular medium and the contributions of uptake and Na^+/Ca^{2+} exchanger mechanisms to Ca^{2+} removal are similar to published reports (2). Thus our simulations offer an acceptable agreement between model and data in current-clamp and voltage-clamp settings.

The robustness of our model is illustrated by its ability to simulate the rate-dependent variability of the action potential. Although the magnitudes of individual ionic currents vary greatly over the 0.2- to 3.0-Hz range of stimulus rates employed, the model is able to mimic action potentials and instantaneous I - V trajectories quite closely.

The predictive capability of our model is also illustrated by simulations of the response to premature stimuli. Waveshape recovery in the model-generated premature stimulus response is qualitatively similar to that recorded from human atrium (Fig. 5 in Ref. 38). The model predicts the timing of the classically defined absolute and relative refractory periods of the cardiac

cycle. It suggests that these periods are dominated by I_{Na} reactivation and that this relationship might be used to probe the physiological behavior of I_{Na} in a current-clamp setting.

Genesis of the Rabbit Atrial Action Potential

Experimental studies in single myocytes have provided considerable information concerning the properties of the various ionic currents in the cardiac sarcolemma. As a result, the roles of certain currents (e.g., I_t) in the genesis of the action potential have been clarified (46). However, additional data are required to understand the genesis of the action potential and its modulation by rate in quantitative terms.

Boyett and Jewell (11) proposed two types of mechanisms to account for the rate dependence of the action potential. Incomplete recovery of gated sarcolemmal currents is postulated to alter the size of various currents from beat to beat. This would occur as incomplete reactivation for the fast Na^+ (I_{Na}), long-lasting Ca^{2+} ($I_{Ca,L}$), and transient outward (I_t) currents. Slow activating currents such as the delayed rectifier K^+ current (I_K) would undergo incomplete deactivation. A somewhat slower mechanism centers around the accumulation or depletion of ions within intra- and extracellular compartments. Rate-dependent changes in the concentrations of certain ions, particularly intracellular Na^+ and Ca^{2+} as well as K^+ and Ca^{2+} within extracellular cleft spaces, would alter ion-sensitive currents such as the Na^+-K^+ pump (I_{NaK}), Na^+/Ca^{2+} exchanger (I_{NaCa}), and Ca^{2+} -activated K^+ current ($I_{K,Ca}$). Although potentially significant *in vivo*, the accumulation/depletion mechanism is less likely to influence rate-dependent APW changes in the enzymatically isolated myocyte preparation.

This model offers one hypothesis as to how the action potential and rate-dependent APW variations may be generated in rabbit atrial cells. It predicts that, at a physiological rate of stimulation, ionic currents contribute significantly to the action potential in the following approximate order: I_{Na} , I_t , $I_{Ca,L}$, I_{NaCa} , $I_{K,s}$, $I_{K,r}$, $I_{K,l}$. Other background currents such as I_{NaK} are predicted to contribute throughout all phases of the action potential.

The studies by Boyett et al. (7, 8, 11) and others (46, 74) suggest that the rate-dependent APW changes of the rabbit atrial myocyte may be attributed mainly to changes in I_t because of its incomplete reactivation. Our model has accounted for the slow gating kinetics of those major ionic currents (I_{Na} , I_t , $I_{Ca,L}$, and I_K) associated with incomplete recovery phenomena. Without also modeling the effects of ionic accumulation/depletion, the model is nevertheless able to accurately simulate the rate-dependent APW variation of the enzymatically isolated rabbit atrial myocyte. Moreover, the inclusion of all the relevant slow kinetics in the model has allowed more complex rate-dependent effects (e.g., on $I_{Ca,L}$, I_K , and I_{Na}) to be considered.

As an illustration, we compare the rate-dependent modulation of I_{Na} to the modulation of I_{Na} that is elicited by premature stimulation. In the former case,

increasing the stimulus frequency from 0.2 to 3.0 Hz decreases I_{Na} . This occurs as a result of a rate-dependent elevation of the MDP and not incomplete inactivation, which we have found becomes substantial at very high stimulus rates (>3 Hz; not shown). Because the peak overshoot increases substantially with stimulus rate, I_{Na} is unlikely to be responsible for this change. However, after a premature stimulus, the action potential recovers with a time course that mirrors that of I_{Na} reactivation. A consequence of this is that the absolute refractory period depends largely on the time required for repolarization to -55 mV, the threshold for reactivation of I_{Na} (Fig. 2A). This interval changes very little in our action potential data (Fig. 13). Therefore, our model predicts the absolute refractory period to be nearly independent of stimulus rate over 0.2 to 3.0-Hz stimulation, despite pronounced changes in the APW over this same range.

Comparison With Previous Cardiac Models

Our model of the rabbit atrial myocyte shares many qualitative similarities with earlier cardiac models such as the Beeler-Reuter (BR) (4), DN (28), Nordin (NOR) (93), HN (56), Luo and Rudy (LR1 and LR2) (75–77), Rasmusson et al. (RCG) (98, 99), and Demir et al. (DCMG) (26). Each of these models has provided descriptions of Na^+ , K^+ , and Ca^{2+} currents and has been utilized to simulate electrophysiological responses of interest. There are, however, several differences, which are noted below.

Model objectives. The development of our rabbit atrial cell model was motivated by the proliferation of voltage-clamp data recorded from these isolated cells and the similarity of electrophysiological and pharmacological responses in rabbit and human atrium (46). Our objective of simulating action potentials in a quantitative manner also differs from the approaches of most earlier cardiac models. For instance, neither the DN nor the HN model attempts to mimic action potentials quantitatively. The LR1 and LR2 models present some data with respect to membrane currents but make no direct comparison of simulated and recorded action potentials. The NOR model, a derivative of the DN formulation, adopts an intermediate approach, inasmuch as some qualitative comparisons are provided between simulated and recorded action potentials (93). In this regard, the RCG bullfrog models (98, 99) and the SA nodal cell DCMG model (26) are more closely related to the present rabbit model, in that membrane components and overall action potential responses are compared directly with physiological data.

Single cell vs. multicellular models. We have provided descriptions of membrane currents on the basis of single cell recordings from isolated rabbit cardiomyocytes and have incorporated anatomic data describing the ultrastructural geometry of the rabbit myocyte. A similar approach was employed in the DCMG model for the rabbit SA nodal cell (26) and the LR1 and LR2 models for the guinea pig ventricular cell (75–77). In contrast, the BR, DN, and HN models are based on data from multicellular or fiber preparations (4, 28, 56).

Compartments and intracellular ion mass balances. The DN, HN, NOR, RCG, and DCMG models provide compartmental descriptions to consider mass-balance issues, whereas the BR and LR1 models do not. Similar balances in our atrial cell model allow the simulation of dynamic changes in intracellular Na^+ , K^+ , and Ca^{2+} as well as SR Ca^{2+} concentrations. The recent LR2 model calculates transients only for Ca^{2+} (76). We have also carefully considered ionic homeostasis within our model. As a result, intracellular Na^+ concentration differs by ~ 2.8 mM between the quiescent and actively stimulated cell.

Ca^{2+} buffering and material balance. This and several previous models (RCG, DCMG, HN, and LR2) take into account the buffering of intracellular Ca^{2+} by Ca^{2+} -binding proteins. A notable exception is the NOR model (93), which does not consider these buffering effects in a direct manner. Aside from the NOR model, the models account for troponin and calmodulin buffering within the intracellular medium. The LR2, DCMG, and our atrial cell model also account for the binding of Ca^{2+} to calsequestrin within the release compartment of the SR. This buffering is not present in the HN model. In addition, the HN and LR2 models assume instantaneous binding of Ca^{2+} to various buffers; in contrast, we have modeled the dynamics of buffer binding. These kinetics are slow enough to significantly affect the waveshape of the $[\text{Ca}^{2+}]_i$ transient during the action potential. They are important in accurately describing rapid changes in $[\text{Ca}^{2+}]_i$, for instance, after SR Ca^{2+} release.

Several earlier models (BR and LR1) do not contain adequate descriptions of the intracellular Ca^{2+} balance. That is, they provide no description of Ca^{2+} buffering or Ca^{2+} handling by the Ca^{2+} extrusion pump (I_{CaP}), $\text{Na}^+/\text{Ca}^{2+}$ exchanger (I_{NaCa}), or uptake and release of Ca^{2+} by the SR. These deficits were recognized and have been addressed in a recently published phase 2 model (LR2) (76, 77), which now includes descriptions of I_{CaP} , I_{up} , and I_{rel} . Adequate characterization of the intracellular Ca^{2+} balance of the cardiac cell is most important in achieving a proper functional description of the cell under a variety of different conditions (e.g., rate and temperature) as well as under abnormal conditions such as ischemia and arrhythmia.

SR. Hilgemann and Noble (56) developed a compartmental model of the SR to account for Ca^{2+} uptake and release phenomena. In general terms, the structural components of our atrial model are similar to those of the HN model. Our model differs from the HN model, however, in the emphasis we have placed on a single cell characterization. Consequently, the sizes and dynamics of SR Ca^{2+} fluxes have been adjusted to appropriate levels for the rabbit atrial myocyte. Our SR Ca^{2+} model also accounts for the buffering of Ca^{2+} by calsequestrin, an important phenomenon omitted in the HN model but included in the DCMG and LR2 models. Because histological investigations have shown that the bullfrog atrial myocyte does not have a transverse tubular system and possesses very little SR (62, 63), previous models of the bullfrog atrial and sinus venosus

cells (98, 99) did not include these intracellular organelles.

The LR2 model provides a new two-compartment model of the SR Ca^{2+} fluxes that differs significantly in form and function from those of the HN model. The HN model includes a voltage-dependent term in the activation of SR Ca^{2+} release that mimics "local CICR" when the "common pool" (109) $[\text{Ca}^{2+}]_i$ trigger signal is small. In the LR2 model, I_{rel} has no explicit dependence on membrane potential. In addition, Hilgemann and Noble described the SR Ca^{2+} release channel mechanistically by using a three-state model formulated with use of ordinary differential equations. The LR2 model does not describe the SR release current mechanistically, because their formulation 1) utilizes different models of Ca^{2+} release depending on stimulation conditions and 2) describes the release signal empirically as a product of time-dependent exponential terms.

Sarcolemmal currents. The formulations for a number of time- and voltage-dependent membrane currents also differ in quantitative and qualitative aspects from earlier models. Qualitatively, we have attempted to characterize the gating of membrane currents throughout the cardiac cycle, accounting for slow recovery from inactivation within each of the three largest membrane currents (I_{Na} , I_t , and $I_{\text{Ca,L}}$) in the rabbit atrial myocyte. Quantitatively, we have supplied a basis in single cell data for each ionic current described in the rabbit atrial myocyte. Some important points of distinction between this and previous models are as follows.

1) I_{Na} . We have included a slowly inactivating component (h_2) in our description of I_{Na} to model the participation of I_{Na} in the plateau. This component is mentioned but not included in the DN or the later HN model. In the LR1 and LR2 models (75–77), a product of two inactivating gating variables is used. Although the second gating variable conveniently limits the size of I_{Na} during repolarization, the multiplicative form does not produce biexponential inactivation or reactivation responses under voltage-clamp conditions.

2) I_t . We have concentrated on developing accurate mathematical expressions for the steady-state and time-dependent behavior of I_t on the basis of physiological data. In particular, we have provided simulated fits to the entire set of transients evoked from a standard voltage-clamp protocol. Previous models, in contrast, usually represent only information derived from exponential fits to a portion of the voltage-clamp response and are therefore unable to simulate this response.

3) $I_{\text{Ca,L}}$. We have simulated measurements of the steady-state and time-dependent properties of $I_{\text{Ca,L}}$ using a single Ca^{2+} -independent inactivation gating variable. Our formulation therefore differs from the HN and LR descriptions, which included a Ca^{2+} -dependent modulation of inactivation. Furthermore, we have found a monoexponential description of $I_{\text{Ca,L}}$ to be adequate in describing the rabbit atrial plateau. It is possible that a multiexponential Ca^{2+} -dependent formulation may prove more suitable for cells with a longer APD, e.g., ventricular cells, or for situations in which SR Ca^{2+} release is significantly modulated.

4) I_K . We have included data-based descriptions of recently identified (49, 102, 103) slow and fast ($I_{K,s}$ and $I_{K,r}$) delayed K^+ currents. Earlier cardiac models (DN, HN, RCG, and LR2) included only a single type of I_K in the membrane model. Our description of $I_{K,s}$ is qualitatively similar to the classic delayed rectifier.

5) I_{K1} . We have simulated the available experimental data for the ion-transfer behavior of I_{K1} and illustrated several functional roles for I_{K1} in atrial tissue. Agreement between model-generated and measured passive cell properties, such as RP and R_{in} , was achieved using an appropriate current density for I_{K1} . The resulting conductance (G_{K1}) allowed a rather small peak current comparable in size to I_{NaK} . Our model therefore differs from the HN I_{K1} current (which did not reverse at E_K) and from previous models (DN, HN, LR, and LR2), which did not utilize R_{in} measurements to help define the background state (28, 56, 75, 76, 98, 99).

6) $I_{B,Cl}$. We have included a recently identified background current, thought to be carried by Cl^- , to explain the steady-current response in voltage-clamp experiments designed to measure I_t (29). Although Cl^- currents have been described in mammalian cardiac myocytes (54, 55), a background Cl^- current has not been included in earlier models.

7) *Background currents.* Consideration has been given in our model to accurately representing the background or resting state of the rabbit atrial myocyte by use of expressions for I_{NaCa} , I_{NaK} , I_{CaP} , and I_B currents. These currents were not included in the LR1 model, although they were added in the recent LR2 model. We have also constrained the size of certain currents, such as I_{NaK} and I_{K1} , to reflect measured properties of the background state. A 3:2 coupling ratio of Hill coefficients was utilized for Na^+ and K^+ transport, yielding the electrogenic current I_{NaK} , rather than the 1:1 ratio of the HN model.

Model Limitations

Our model represents significant improvements in a number of areas; nevertheless it must also be considered in the context of known limitations.

Very limited experimental data on the $[Ca^{2+}]_i$ transient during the action potential are available. The modified HN description (56) of the SR included in our model qualitatively mimics the phenomenon of CICR and provides for a relatively stable interaction between transmembrane, SR uptake, and SR release Ca^{2+} fluxes. The $[Ca^{2+}]_i$ transient predicted by our model rises to 1 μM within 10 ms and declines to 200 nM within 50 ms. This relatively "impulsive" transient has a shorter duration than many Ca^{2+} -sensitive recordings made at room temperature (6). However, when the filtering and buffering effects of the dye measurement are considered, it is comparable in shape and extent to some recordings made at a similar temperature (Fig. 3 in Ref. 53). Nevertheless, the available data do not provide a sufficient basis for modeling the behavior of various intracellular Ca^{2+} handling mechanisms quantitatively.

Mass balances for ions other than Na^+ , K^+ , and Ca^{2+} (i.e., Cl^- and H^+) are not considered in this model, even

though a Cl^- current is included in the sarcolemma. Consequently, the model applies only to conditions in which the concentrations of these ions remain fixed (i.e., constant E_{Cl} and pH).

Although our descriptions of the major rabbit atrial ionic currents have been based extensively on single cell data, certain limitations apply to each formulation.

1) For instance, the transient outward K^+ current was simulated quite closely with a sum of I_t and $I_{B,Cl}$. Nevertheless, we cannot rule out contributions from other K^+ current subtypes, such as a rapidly activating delayed rectifier similar to $I_{K,ur}$ in human atrium (37) or I_{K_p} in guinea pig ventricle (114). Such a current could help explain small errors in the steady current fits, as well as the modest empirical deviation of the reversal potential of $I_{B,Cl}$ from E_{Cl} . In addition, $I_{Cl,Ca}$ has not been modeled as a separate current, although to some extent its effects have been incorporated into the formulation for I_t (Fig. 6).

2) Quantitative information on the kinetics of I_{Na} is limited. Suitable data on physiological activation kinetics are lacking, and the available publications do not provide quantitative information on the voltage dependence or interaction of dual time constant inactivation kinetics.

3) There is a lack of quantitative data concerning the mechanisms governing inactivation of $I_{Ca,L}$. Experimental evidence exists for voltage- and Ca^{2+} -dependent regulation (50, 51). In their multicellular atrial fiber model, Hilgemann and Noble (56) included a Ca^{2+} dependence to $I_{Ca,L}$ inactivation. However, despite considerable investigation, the precise nature of the interaction between Ca^{2+} and V in $I_{Ca,L}$ inactivation remains unknown (96). We have not found the absence of multiexponential or Ca^{2+} -dependent inactivation mechanisms to be necessary for modeling the nominal relatively short rabbit atrial action potential. However, such concerns may prove significant if the objective is to study Ca^{2+} overload induced by high $[Ca^{2+}]_o$ (56).

Extrapolations with regard to temperature have been made in the present model to characterize the atrial waveshape at 35°C. We have found this process to be somewhat complex. Whereas scaling adjustments via Q_{10} factors are required to increase reaction kinetics (including gating and binding reactions) at an elevated temperature, such changes have not always proved sufficient. A number of investigators report temperature-dependent shifts in activation and/or inactivation curves. We have found that conductance increases (relative to an earlier 23°C atrial model) have also sometimes been required to yield our present model. Although the latter can be justified on a biophysical basis (increased diffusion rates), consideration of this effect complicates the model analysis and development process.

In general, the quality of fits achieved between model and data in representing individual model elements (e.g., membrane currents), mimicking passive electrical properties, and simulating action potentials is not independent. Instead, requiring a good fit to diverse "current-clamp" data places constraints on the range of

values of "free parameters" in the model (see also Ref. 93). In our model, for instance, the conductance associated with I_{K1} affects the RP, R_{in} , rate of final repolarization of the action potential, and agreement between the model and BaCl₂-sensitive measurements (46) of the size of rabbit atrial I_{K1} . Subject to the overall model paradigm, these properties can determine the size of I_{K1} appropriate to the model. In this sense, the model parameters given in Tables 2–14 represent a "best-achieved" representation of the electrophysiological responses of the rabbit atrial myocyte.

APPENDIX A

Computational Aspects and Data Analysis

The simulations were obtained by forward integration of the equations in Tables 2–13 with use of a Runge-Kutta-Merson algorithm (44) with a variable step size. Double-precision floating-point arithmetic was used in all calculations to minimize round-off errors due to finite precision. This was necessary to accurately integrate the relatively stiff system of differential equations, the time constants of which vary from 14.6 μ s (I_{Na} activation kinetics) to 8 s (slowest reactivation component of I_t). The accuracy of membrane voltage, ion concentration, and gating variable values was guaranteed by requiring that the local error of each state variable satisfy a relative error constraint. The code was developed in the C programming language under the Unix operating system, and simulations were performed on Sun Microsystems Sparc workstation (Sparc 2, IPX, SLC) platforms. Simulation of the action potentials typically required ~3.5 min of execution time on a Sun IPX platform.

The atrial action potentials represent the typical steady-state waveshapes achieved at each stimulus rate after stimulation for several tens of seconds. Action potentials were recorded at 34–35°C in the laboratory of W. R. Giles from enzymatically isolated rabbit atrial cells. The action potentials were digitally sampled (2-kHz sampling rate, 12-bit quantization), and the raw data were adjusted to facilitate comparison with the model. Specifically, the integer output from analog-to-digital conversion of the membrane voltage waveform was scaled by the analog-to-digital gain factor to achieve an appropriate range of excursion (peak overshoot) of the output values. The data were then offset by -10.5 mV to correct for tip potential and agree with the nominal resting potential (-71 mV). Data points associated with the stimulus artifact in the raw data were removed, and a Boltzmann expression with an offset was used to fit the remaining rest level and points on the action potential upstroke and to "fill in" an appropriate upstroke phase for the data. However, because of the presence of the stimulus artifact and the low sampling rate (2 kHz) used in the action potential recordings, no attempt was made to analyze the action potential upstroke in the phase plane.

To obtain a suitable approximation of I_{net} for use in I-V trajectories, the slow phases of repolarization of the action potential data were processed through a Butterworth filter. The reconstructed action potential was median filtered before and after differentiation to limit noise associated with differentiation, which was performed using difference algorithms. Correctness of the derived repolarization currents was verified by comparing the unfiltered action potential repolarization phase with the waveshape predicted by integrating repolarization currents from the point of peak overshoot by use of Simpson's rule.

APPENDIX B

Tables 2–16 present a complete set of equations, parameter values, and initial conditions used in the model. Unless otherwise specified, model parameters are given in standard units: time in seconds, potential in millivolts, concentration in millimolar, current in picoamperes, capacitance in nanofarads, volume in nanoliters, and temperature in Kelvin. The action potentials may be simulated by forward integration of the system of coupled differential equations. The initial conditions given in Table 15 specify the state vector 100 ms before application of the stimulus current, which should consist of a rectangular pulse 650–800 μ s in duration and 2 nA in amplitude. This stimulus provides depolarization of the membrane to just above the threshold for I_{Na} , thus evoking an action potential.

The authors acknowledge the important contributions of Drs. Y. Imaizumi (Nagoya City University, Nagoya, Japan), A. Braun (Dept. of Molecular Pharmacology, Stanford University), and H. Banno (Institute of Biological Science, Mitsui Pharmaceuticals, Chiba, Japan).

D. S. Lindblad is a predoctoral fellow of the W. M. Keck Center for Computational Biology with support through National Library of Medicine Grant T15LM07093. This model development was supported by National Science Foundation Grant BNS-8716568 (J. W. Clark) and National Science Foundation Computers In Science and Engineering CISE-II Grant CCR-8619893. W. R. Giles is supported as a Medical Scientist by the Alberta Heritage Foundation for Medical Research and receives ongoing support from the Canadian Medical Research Council and the Heart and Stroke Foundation of Canada.

Address for reprint requests: J. W. Clark, Dept. of Electrical and Computer Engineering, Rice University, PO Box 1892, Houston, TX 77251-1892.

Received 28 September 1994; accepted in final form 11 March 1996.

REFERENCES

1. Bassani, J. W., R. A. Bassani, and D. M. Bers. Ca²⁺ cycling between sarcoplasmic reticulum and mitochondria in rabbit cardiac myocytes. *J. Physiol. Lond.* 460: 603–621, 1993.
2. Bassani, J. W., R. A. Bassani, and D. M. Bers. Relaxation in rabbit and rat cardiac cells: species-dependent differences in cellular mechanisms. *J. Physiol. Lond.* 476: 279–293, 1994.
3. Bean, B. P. Two kinds of calcium channels in canine atrial cells. Differences in kinetics, selectivity, and pharmacology. *J. Gen. Physiol.* 86: 1–30, 1985.
4. Beeler, G., and H. Reuter. Reconstruction of the action potential of ventricular myocardial fibers. *J. Physiol. Lond.* 286: 177–210, 1977.
5. Berne, R. M., and M. N. Levy. *Physiology* (2nd ed.). St. Louis, MO: Mosby, 1988, p. 22–30.
6. Beuckelmann, D. J., and W. G. Wier. Mechanism of release of calcium from sarcoplasmic reticulum of guinea-pig cardiac cells. *J. Physiol. Lond.* 405: 233–255, 1988.
7. Boyett, M. Effect of rate-dependent changes in the transient outward current on the action potential in sheep Purkinje fibres. *J. Physiol. Lond.* 319: 23–41, 1981.
8. Boyett, M. A study of the effect of the rate of stimulation on the transient outward current in sheep cardiac Purkinje fibres. *J. Physiol. Lond.* 319: 1–22, 1981.
9. Boyett, M., and D. Fedida. Changes in the electrical activity of dog cardiac Purkinje fibers at high heart rates. *J. Physiol. Lond.* 350: 361–391, 1984.
10. Boyett, M. R., and D. Fedida. The effect of heart rate on the membrane currents of isolated sheep Purkinje fibres. *J. Physiol. Lond.* 399: 467–491, 1988.
11. Boyett, M., and B. Jewell. Analysis of the effects of changes in rate and rhythm upon electrical activity in the heart. *Prog. Biophys. Mol. Biol.* 36: 1–52, 1980.
12. Braun, A. P., R. B. Clark, and W. R. Giles. Ca²⁺-independent transient outward current in mammalian heart. In: *Molecular*

- Physiology and Pharmacology of Cardiac Ion Channels and Transporters*, edited by M. Morad, Y. Kurachi, A. Noma, and M. Hosoda. Amsterdam: Kluwer, 1996, p. 141–168.
13. **Campbell, D. L., W. R. Giles, J. R. Hume, and E. F. Shibata.** Inactivation of calcium current in bull-frog atrial myocytes. *J. Physiol. Lond.* 403: 287–315, 1988.
 14. **Campbell, D., R. Rasmusson, Y. Qu, and H. C. Strauss.** The calcium-independent transient outward potassium current in isolated ferret right ventricular myocytes. *J. Gen. Physiol.* 101: 571–601, 1993.
 15. **Cannell, M., and D. Allen.** Model of calcium movements during activation in the sarcomere of frog skeletal muscle. *Biophys. J.* 45: 913–925, 1984.
 16. **Carafoli, E.** Intracellular calcium regulation, with special attention to the role of the plasma membrane calcium pump. *J. Cardiovasc. Pharmacol.* 12, Suppl. 3: S77–S84, 1988.
 17. **Carmeliet, E.** Voltage- and time-dependent block of the delayed K^+ current in cardiac myocytes by dofetilide. *J. Pharmacol. Exp. Ther.* 262: 809–817, 1992.
 18. **Caroni, P., M. Zurini, A. Clark, and E. Carafoli.** Further characterization and reconstitution of the purified Ca-pumping ATPase of heart sarcolemma. *J. Biol. Chem.* 258: 7305–7310, 1983.
 19. **Chapman, R. A., E. A. Johnson, and J. M. Kootsey.** Electrical and biochemical properties of an enzyme model of the sodium pump. *J. Membr. Biol.* 74: 139–153, 1983.
 20. **Clark, R. B., and W. Giles.** Sodium current in single cells from bullfrog atrium: voltage dependence and ion transfer properties. *J. Physiol. Lond.* 391: 235–265, 1987.
 21. **Clark, R., W. Giles, and Y. Imaizumi.** Properties of the transient outward current in rabbit atrial cells. *J. Physiol. Lond.* 405: 147–168, 1988.
 22. **Clay, J., A. Ogbaghebriel, T. Paquette, B. Sasyniuk, and A. Shrier.** A quantitative description of the E-4031-sensitive repolarization current in rabbit ventricular myocytes. *Biophys. J.* 69: 1830–1837, 1995.
 23. **Cohen, I. S., N. B. Datyner, G. A. Gintant, N. K. Mulrine, and P. Pennefather.** Properties of an electrogenic sodium-potassium pump in isolated canine Purkinje myocytes. *J. Physiol. Lond.* 383: 251–267, 1987.
 24. **Colatsky, T.** Voltage clamp measurements of sodium channel properties in rabbit cardiac Purkinje fibers. *J. Physiol. Lond.* 305: 215–234, 1980.
 25. **Colatsky, T. J., C. H. Follmer, and C. F. Starmer.** Channel specificity in antiarrhythmic drug action. Mechanism of potassium channel block and its role in suppressing and aggravating cardiac arrhythmias. *Circulation* 82: 2235–2242, 1990.
 26. **Demir, S., J. Clark, C. Murphrey, and W. Giles.** A mathematical model of a rabbit sinoatrial node cell. *Am. J. Physiol.* 266 (Cell Physiol. 35): C832–C852, 1994.
 27. **Désilets, M., and C. M. Baumgarten.** Na^+ , K^+ , and Cl^- activities in ventricular myocytes isolated from rabbit heart. *Am. J. Physiol.* 251 (Cell Physiol. 20): C197–C208, 1986.
 28. **DiFrancesco, D., and D. Noble.** A model of cardiac electrical activity incorporating ionic pumps and concentration changes. *Philos. Trans. R. Soc. Lond. Biol. Sci.* 307: 353–398, 1985.
 29. **Duan, D., B. Fermini, and S. Nattel.** Sustained outward current observed after I_{to1} inactivation in rabbit atrial myocytes is a novel Cl^- current. *Am. J. Physiol.* 263 (Heart Circ. Physiol. 32): H1967–H1971, 1992.
 30. **Earm, Y., W. Ho, and I. So.** Inward current generated by Na-Ca exchange during the action potential in single atrial cells of the rabbit. *Proc. R. Soc. Lond. Ser. B Biol. Sci.* 240: 61–81, 1990.
 31. **Earm, Y., and D. Noble.** A model of the single atrial cell: relation between calcium current and calcium release. *Proc. R. Soc. Lond. Ser. B Biol. Sci.* 240: 83–96, 1990.
 32. **Eisner, D. A., and T. W. Smith.** The Na-K pump and its effectors in cardiac muscle. In: *The Heart and Cardiovascular System: Scientific Foundations* (2nd ed.), edited by H. A. Fozzard, E. Haber, R. B. Jennings, A. M. Katz, and H. E. Morgan. New York: Raven, 1992, p. 863–902.
 33. **Fabiato, A.** Simulated calcium current can both cause calcium loading in and trigger calcium release from the sarcoplasmic reticulum of a skinned canine cardiac Purkinje cell. *J. Gen. Physiol.* 85: 291–320, 1985.
 34. **Fabiato, A.** Appraisal of the physiological relevance of two hypotheses for the mechanism of calcium release from the mammalian cardiac sarcoplasmic reticulum: calcium-induced release versus charge-coupled release. *Mol. Cell. Biochem.* 89: 135–140, 1989.
 35. **Fedida, D., and W. Giles.** Regional variations in the action potentials and transient outward current in myocytes isolated from the rabbit left ventricle. *J. Physiol. Lond.* 442: 191–209, 1991.
 36. **Fedida, D., Y. Shimoni, and W. Giles.** α -Adrenergic modulation of the transient outward current in rabbit atrial myocytes. *J. Physiol. Lond.* 423: 257–277, 1990.
 37. **Fedida, D., B. Wible, Z. Wang, B. Fermini, F. Faust, S. Nattel, and A. M. Brown.** Identity of a novel delayed rectifier current from human heart with a cloned K^+ channel current. *Circ. Res.* 73: 210–216, 1993.
 38. **Fermini, B., Z. Wang, D. Duan, and S. Nattel.** Differences in rate dependence of transient outward current in rabbit and human atrium. *Am. J. Physiol.* 263 (Heart Circ. Physiol. 32): H1747–H1754, 1992.
 39. **Follmer, C. H., R. E. ten Eick, and J. Z. Yeh.** Sodium current kinetics in cat atrial myocytes. *J. Physiol. Lond.* 384: 169–197, 1987.
 40. **Fozzard, H. A., and D. A. Hanck.** Sodium channels. In: *The Heart and Cardiovascular System: Scientific Foundations* (2nd ed.), edited by H. A. Fozzard, E. Haber, R. B. Jennings, A. M. Katz, and H. E. Morgan. New York: Raven, 1992, p. 1091–1119.
 41. **Gadsby, D. C., J. Kimura, and A. Noma.** Voltage-dependence of the Na/K pump in isolated heart cells. *Nature Lond.* 315: 63–65, 1985.
 42. **Gadsby, D. C., and M. Nakao.** Steady-state current-voltage relationship of the Na/K pump in guinea pig ventricular myocytes. *J. Gen. Physiol.* 94: 511–537, 1989.
 43. **Gadsby, D., and M. Nakao.** $[Na]$ and $[K]$ dependence of the Na/K pump current-voltage relationship in guinea pig ventricular myocytes. *J. Gen. Physiol.* 94: 539–565, 1989.
 44. **Gerald, C., and P. Wheatley.** *Applied Numerical Analysis*. Reading, MA: Addison-Wesley, 1989.
 45. **Giles, W., and Y. Imaizumi.** Comparison of potassium currents in rabbit atrial and ventricular cells. *J. Physiol. Lond.* 405: 123–145, 1988.
 46. **Giles, W., and Y. Shimoni.** Comparison of sodium-calcium exchanger and transient inward currents in single cells from rabbit ventricle. *J. Physiol. Lond.* 417: 465–481, 1989.
 47. **Giles, W., and A. van Ginneken.** A transient outward current in isolated cells from the crista terminalis of rabbit heart. *J. Physiol. Lond.* 368: 243–264, 1985.
 48. **Gilliam, F. R. I., C. F. Starmer, and A. O. Grant.** Blockade of rabbit atrial sodium channels by lidocaine. Characterization of continuous and frequency-dependent blocking. *Circ. Res.* 65: 723–739, 1989.
 49. **Habuchi, Y., X. Han, and W. R. Giles.** Comparison of the hyperpolarization-activated and delayed rectifier currents in rabbit atrioventricular node and sinoatrial node. *Heart Vessels* 9, Suppl.: 203–206, 1995.
 50. **Hadley, R. W., and J. R. Hume.** An intrinsic potential-dependent inactivation mechanism associated with calcium channels in guinea-pig myocytes. *J. Physiol. Lond.* 389: 205–222, 1987.
 51. **Hadley, R. W., and W. J. Lederer.** Ca^{2+} and voltage inactivate Ca^{2+} channels in guinea-pig ventricular myocytes through independent mechanisms. *J. Physiol. Lond.* 444: 257–268, 1991.
 52. **Hagiwara, N., H. Irisawa, and M. Kameyama.** Contribution of two types of calcium currents to the pacemaker potentials of rabbit sino-atrial node cells. *J. Physiol. Lond.* 395: 233–253, 1988.
 53. **Han, S., A. Schiefer, and G. Isenberg.** Ca^{2+} load of guinea-pig ventricular myocytes determines efficacy of brief Ca^{2+} currents as trigger for Ca^{2+} release. *J. Physiol. Lond.* 480: 411–421, 1994.
 54. **Harvey, R. D., C. D. Clark, and J. R. Hume.** Chloride current in mammalian cardiac myocytes. Novel mechanism for autonomic regulation of action potential duration and resting membrane potential. *J. Gen. Physiol.* 95: 1077–1102, 1990.

55. Harvey, R. D., and J. R. Hume. Autonomic regulation of a chloride current in heart. *Science Wash. DC* 244: 983–985, 1989.
56. Hilgemann, D., and D. Noble. Excitation-contraction coupling and extracellular calcium transients in rabbit atrium: reconstruction of basic cellular mechanisms. *Philos. Trans. R. Soc. Lond. Ser. B Biol. Sci.* 230: 163–205, 1987.
57. Hille, B. *Ionic Channels of Excitable Membranes* (2nd ed.). Sunderland, MA: Sinauer, 1992.
58. Hiraoka, M., and S. Kawano. Calcium-sensitive and insensitive transient outward current in rabbit ventricular myocytes. *J. Physiol. Lond.* 410: 187–212, 1989.
59. Hodgkin, A., and A. Huxley. A quantitative description of membrane current and its application to conduction and excitation. *J. Physiol. Lond.* 117: 500–557, 1952.
60. Hodgkin, A., and B. Katz. The effect of sodium ions on the electrical activity of the giant axon of the squid. *J. Physiol. Lond.* 108: 37–77, 1949.
61. Hool, L. C., H. G. Robinson, and H. H. Rasmussen. Effect of captopril treatment on Na^+ , K^+ -pumping in rabbit heart cells (Abstract). *Biophys. J.* 64: A207, 1993.
62. Hume, J., and W. Giles. Active and passive electrical properties of single bullfrog atrial cells. *J. Gen. Physiol.* 78: 19–42, 1981.
63. Hume, J., and W. Giles. Ionic currents in single isolated bullfrog atrial cells. *J. Gen. Physiol.* 81: 153–194, 1983.
64. Imaizumi, Y., and W. Giles. Quinidine-induced inhibition of transient outward current in cardiac muscle. *Am. J. Physiol.* 253 (Heart Circ. Physiol. 22): H704–H708, 1987.
65. Josephson, I. R., J. Sanchez-Chapula, and A. M. Brown. A comparison of calcium currents in rat and guinea pig single ventricular cells. *Circ. Res.* 54: 144–156, 1984.
66. Kawano, S., and M. Hiraoka. Transient outward currents and action potential alterations in rabbit ventricular myocytes. *J. Mol. Cell. Cardiol.* 23: 681–693, 1991.
67. Kimura, J., S. Miyamae, and A. Noma. Identification of sodium-calcium exchange current in single ventricular cells of guinea-pig. *J. Physiol. Lond.* 384: 199–222, 1987.
68. Kleber, A., C. Rieger, and M. Janse. Electrical uncoupling and increase of extracellular resistance after induction of ischemia in isolated, arterially perfused rabbit papillary muscle. *Circ. Res.* 61: 271–279, 1987.
69. Lee, K. S., E. Marban, and R. W. Tsien. Inactivation of calcium channels in mammalian heart cells: joint dependence on membrane potential and intracellular calcium. *J. Physiol. Lond.* 364: 395–411, 1985.
70. Lee, K., and R. Tsien. Reversal of current through calcium channel in dialyzed single heart cells. *Nature Lond.* 297: 498–501, 1982.
71. Lemieux, D. R., F. A. Roberge, and P. Savard. A model study of the contribution of active Na-K transport to membrane repolarization in cardiac cells. *J. Theor. Biol.* 142: 1–34, 1990.
72. Lieberman, M., S. D. Hauschka, Z. W. Hall, B. R. Eisenberg, R. Horn, J. V. Walsh, R. W. Tsien, A. W. Jones, J. L. Walker, and M. Poenie. Isolated muscle cells as a physiological model. *Am. J. Physiol.* 253 (Cell Physiol. 22): C349–C363, 1987.
73. Litovsky, S. H., and C. Antzelevitch. Transient outward current prominent in canine ventricular epicardium but not endocardium. *Circ. Res.* 62: 116–126, 1988.
74. Litovsky, S. H., and C. Antzelevitch. Rate dependence of action potential duration and refractoriness in canine ventricular endocardium differs from that of epicardium: role of the transient outward current. *J. Am. Coll. Cardiol.* 14: 1053–1066, 1989.
75. Luo, C. H., and Y. Rudy. A model of the ventricular cardiac action potential. Depolarization, repolarization, and their interaction. *Circ. Res.* 68: 1501–1526, 1991.
76. Luo, C. H., and Y. Rudy. A dynamic model of the cardiac ventricular action potential. I. Simulations of ionic currents and concentration changes. *Circ. Res.* 74: 1071–1096, 1994.
77. Luo, C. H., and Y. Rudy. A dynamic model of the cardiac ventricular action potential. II. After depolarizations, triggered activity, and potentiation. *Circ. Res.* 74: 1097–1113, 1994.
78. MacLennan, D. H., and P. T. Wong. Isolation of a calcium-sequestering protein from sarcoplasmic reticulum. *Proc. Natl. Acad. Sci. USA* 68: 1231–1235, 1971.
79. Marquardt, D. An algorithm for least-squares estimation of nonlinear parameters. *J. SIAM* 11: 431–441, 1963.
80. Matsuda, J. J., H. Lee, and E. F. Shibata. Enhancement of rabbit cardiac sodium channels by beta-adrenergic stimulation. *Circ. Res.* 70: 199–207, 1992.
81. Mentrard, D., G. Vassort, and R. Fischmeister. Calcium-mediated inactivation of the calcium conductance in cesium-loaded frog heart cells. *J. Gen. Physiol.* 83: 105–131, 1984.
82. Mitchell, R. D., H. K. Simmerman, and L. R. Jones. Ca^{2+} binding effects on protein conformation and protein interactions of canine cardiac calsequestrin. *J. Biol. Chem.* 263: 1376–1381, 1988.
83. Mullins, L. *Ion Transport in the Heart*. New York: Raven, 1981.
84. Muraki, K., Y. Imaizumi, M. Watanabe, Y. Habuchi, and W. R. Giles. Delayed rectifier K^+ current in rabbit atrial myocytes. *Am. J. Physiol.* 269 (Heart Circ. Physiol. 38): H524–H532, 1995.
85. Nakao, M., and D. C. Gadsby. Na^+ and K^+ dependence of the Na/K pump current-voltage relationship in guinea pig ventricular myocytes. *J. Gen. Physiol.* 94: 539–565, 1989.
86. Nathan, R. Two electrophysiologically distinct types of cultured pacemaker cells from the rabbit sinus node. *Am. J. Physiol.* 250 (Heart Circ. Physiol. 19): H325–H329, 1986.
87. Niggli, V., E. Sigel, and E. Carafoli. The purified Ca^{2+} pump of human erythrocyte membranes catalyzes an electroneutral Ca^{2+} - H^+ exchange in reconstituted liposomal systems. *J. Biol. Chem.* 257: 2350–2356, 1982.
88. Nilius, B. Possible functional significance of a novel type of cardiac calcium channel. *Biomed. Biochim. Acta* 45: K37–K45, 1986.
89. Noble, D. The surprising heart: a review of recent progress in cardiac electrophysiology. *J. Physiol. Lond.* 353: 1–50, 1984.
90. Noble, D. Sodium-calcium exchange and its role in generating electric current. In: *Cardiac Muscle: Excitation and Regulation of Contraction*, edited by R. Nathan. London: Academic, 1986, p. 171–200.
91. Noble, D., and S. Noble. A model of sino-atrial node electrical activity based on a modification of the DiFrancesco-Noble (1984) equations. *Proc. R. Soc. Lond. Ser. B Biol. Sci.* 222: 295–304, 1984.
92. Noma, A., K. Yanigahara, and H. Irisawa. Reconstruction of sinoatrial node pacemaker potential based on voltage clamp experiments. *Jpn. J. Physiol.* 30: 841–857, 1980.
93. Nordin, C. Computer model of membrane current and intracellular Ca^{2+} flux in the isolated guinea pig ventricular myocyte. *Am. J. Physiol.* 265 (Heart Circ. Physiol. 34): H2117–H2136, 1993.
94. Ostwald, T. J., and D. H. MacLennan. Isolation of a high affinity calcium-binding protein from sarcoplasmic reticulum. *J. Biol. Chem.* 249: 974–979, 1974.
95. Page, E. Quantitative ultrastructural analysis in cardiac membrane physiology. *Am. J. Physiol.* 235 (Cell Physiol. 4): C147–C158, 1978.
96. Pelzer, D., S. Pelzer, and T. F. McDonald. Properties and regulation of calcium channels in muscle cells. *Rev. Physiol. Biochem. Pharmacol.* 114: 107–207, 1990.
97. Potter, J. D., and H. G. Zott. The role of actin in modulating Ca^{2+} binding to troponin (Abstract). *Biophys. J.* 37: 43A, 1982.
98. Rasmusson, R., J. Clark, W. Giles, K. Robinson, D. Campbell, R. Clark, and E. Shibata. A mathematical model of electrophysiological activity in a bullfrog atrial cell. *Am. J. Physiol.* 259 (Heart Circ. Physiol. 28): H370–H389, 1990.
99. Rasmusson, R., J. Clark, W. Giles, E. Shibata, and D. Campbell. A mathematical model of the single bullfrog cardiac pacemaker cell. *Am. J. Physiol.* 259 (Heart Circ. Physiol. 28): H352–H369, 1990.
100. Robertson, S. P., J. D. Johnson, and J. D. Potter. The time-course of Ca^{2+} exchange with calmodulin, troponin, parvalbumin, and myocin in response to a transient increase in Ca^{2+} . *Biophys. J.* 34: 559–569, 1982.
101. Sakakibara, Y., J. A. Wasserstrom, T. Furukawa, H. Jia, C. E. Arentzen, R. S. Hartz, and D. H. Singer. Characterization of the sodium current in single human atrial myocytes. *Circ. Res.* 71: 535–546, 1992.

102. **Sanguinetti, M. C., and N. K. Jurkiewicz.** Two components of cardiac delayed rectifier K^+ current. Differential sensitivity to block by class III antiarrhythmic agents. *J. Gen. Physiol.* 96: 195–215, 1990.
103. **Sanguinetti, M. C., and N. K. Jurkiewicz.** Delayed rectifier outward K^+ current is composed of two currents in guinea pig atrial cells. *Am. J. Physiol.* 260 (*Heart Circ. Physiol.* 29): H393–H399, 1991.
104. **Shibasaki, T.** Conductance and kinetics of delayed rectifier potassium channels in nodal cells of the rabbit heart. *J. Physiol. Lond.* 387: 227–250, 1987.
105. **Shibata, E., Y. Morooka, and W. R. Giles.** An electrogenic Na^+/K^+ pump current in individual bullfrog atrial myocytes (Abstract). *Biophys. J.* 45: 136A, 1984.
106. **Shimoni, Y., H. Banno, and R. B. Clark.** Hyperthyroidism selectively modified a transient potassium current in rabbit ventricular and atrial myocytes. *J. Physiol. Lond.* 457: 369–389, 1992.
107. **Shimoni, Y., R. B. Clark, and W. R. Giles.** Role of an inwardly rectifying potassium current in rabbit ventricular action potential. *J. Physiol. Lond.* 448: 709–727, 1992.
108. **Solaro, R. J., R. M. Wise, J. S. Shiner, and F. N. Briggs.** Calcium requirements for cardiac myofibrillar activation. *Circ. Res.* 34: 525–530, 1974.
109. **Stern, M. D.** Theory of excitation-contraction coupling in cardiac muscle. *Biophys. J.* 63: 497–517, 1992.
110. **Tanaka, I., T. Tosaka, K. Saito, II. Shin-mura, and T. Saito.** Changes in the configuration of the rabbit atrial action potential after various periods of rest. *Jpn. J. Physiol.* 17: 487–504, 1967.
111. **Veldkamp, M. W., A. C. van Ginneken, and L. N. Bouman.** Single delayed rectifier channels in the membrane of rabbit ventricular myocytes. *Circ. Res.* 72: 865–878, 1993.
112. **Wendt, D. J., C. F. Starmer, and A. O. Grant.** Na channel kinetics remain stable during perforated-patch recordings. *Am. J. Physiol.* 263 (*Cell Physiol.* 32): C1234–C1240, 1992.
113. **Wier, W. G., T. M. Egan, J. R. López-López, and C. W. Balke.** Local control of excitation-contraction coupling in rat heart cells. *J. Physiol. Lond.* 474: 463–471, 1994.
114. **Yue, D. T., and E. Marban.** A novel cardiac potassium channel that is active and conductive at depolarized potentials. *Pfluegers Arch.* 413: 127–133, 1988.
115. **Zygmunt, A., and W. Gibbons.** Calcium-activated chloride current in rabbit ventricular myocytes. *Circ. Res.* 68: 424–438, 1991.
116. **Zygmunt, A. C., and W. R. Gibbons.** Properties of the calcium-activated chloride current in heart. *J. Gen. Physiol.* 99: 391–414, 1992.

